Benchmarking Dust Emission Models in M101

Jérémy Chastenet[1] , Karin Sandstrom[1] , I-Da Chiang (江宜達)[1] , Brandon S. Hensley[2] , Bruce T. Draine[2] ,
Karl D. Gordon[3,4] , Eric W. Koch[5] , Adam K. Leroy[6] , Dyas Utomo[6] , and Thomas G. Williams[7]

[1] Center for Astrophysics and Space Sciences, Department of Physics, University of California, San Diego 9500 Gilman Drive, La Jolla, CA 92093, USA
jchastenet@ucsd.edu

[2] Princeton University Observatory, Peyton Hall, Princeton, NJ 08544-1001, USA
[3] Space Telescope Science Institute, 3700 San Martin Drive, Baltimore, MD 21218, USA
[4] Sterrenkundig Observatorium, Universiteit Gent, Gent, Belgium
[5] University of Alberta, Department of Physics, 4-183 CCIS, Edmonton, AB T6G 2E1, Canada
[6] Department of Astronomy, The Ohio State University, 4055 McPherson Laboratory, 140 West 18th Avenue, Columbus, OH 43210, USA
[7] Max Planck Institut für Astronomie, Königstuhl 17, D-69117 Heidelberg, Germany

Abstract

We present a comparative study of four physical dust models and two single-temperature modified blackbody models by fitting them to the resolved WISE, Spitzer, and Herschel photometry of M101 (NGC 5457). Using identical data and a grid-based fitting technique, we compare the resulting dust and radiation field properties derived from the models. We find that the dust mass yielded by the different models can vary by up to a factor of 3 (factor of 1.4 between physical models only), although the fits have similar quality. Despite differences in their definition of the carriers of the mid-IR aromatic features, all physical models show the same spatial variations for the abundance of that grain population. Using the well-determined metallicity gradient in M101 and resolved gas maps, we calculate an approximate upper limit on the dust mass as a function of radius. All physical dust models are found to exceed this maximum estimate over some range of galactocentric radii. We show that renormalizing the models to match the same Milky Way high-latitude cirrus spectrum and abundance constraints can reduce the dust mass differences between models and bring the total dust mass below the maximum estimate at all radii.

1. Introduction

Dust grains play key roles in processes that shape the interstellar medium (ISM) and galaxy evolution. They release photoelectrons that participate in heating gas (e.g., Wolfire et al. 1995; Weingartner & Draine 2001a; Croxall et al. 2012), they shield dense molecular clouds from stellar UV radiation and aid their collapse (e.g., Fumagalli et al. 2010; Byrne et al. 2019), they catalyze a number of chemical reactions, and they offer a surface area for the production of H_2 (e.g., Bron et al. 2014; Castellanos et al. 2018; Thi et al. 2020, see also a review by Wakelam et al. 2017). It is therefore critically important to understand dust properties and abundance, and how dust affects these processes.

One main way to infer dust properties in external galaxies is to interpret infrared (IR) spectral energy distributions (SEDs) with the aid of dust models. The near-to-mid-IR part of the spectrum is dominated by the emission of stochastically heated grains that do not achieve a steady-state equilibrium with the incident radiation field. At longer wavelengths, the emission is almost entirely due to grains in thermal equilibrium, with a large enough radius to be constantly receiving and emitting photons. In this regime, the steady-state grain temperature is set by the strength of the incident radiation field.

Modified blackbody models are a convenient parametric representation of the emission from large grains in thermal equilibrium. As such, they provide good fits to the far-IR SED and yield satisfactory dust masses if correctly calibrated (e.g., Bianchi 2013), because these grains contain most of the dust mass. Large grains in thermal equilibrium are reasonably well described by a single temperature, in which case their emission

can be represented by a blackbody radiation, B_ν, modified by an effective grain opacity, $\kappa_\nu(\lambda)$, so that the grain emission $I_\nu \propto \kappa_\nu(\lambda) B_\nu(\lambda, T)$. The opacity as a function of wavelength is often described with a power law with spectral index β, such that $\kappa_\nu = \kappa_0 (\nu/\nu_0)^\beta$. Several variations to the modified blackbody model have been used to fit the far-IR SED, for example, multiple dust populations having different temperatures and β, or a different functional form for κ_ν such as a broken power law.

Physical dust models aim to reproduce the IR emission, extinction, and depletions, among other observations, with a self-consistent description of dust properties. Building these models requires specifying grain sizes, shapes, and chemical composition, which lead to optical properties and heat capacities. These grain populations are then illuminated by a radiation field with a specified intensity and spectrum. Once the radiation field is modeled, one can compare the predicted and observed dust emission. Dust extinction measured toward specific lines of sight (not high A_V) helps constrain the size distribution of grains, their composition, and total mass relative to H (e.g., Weingartner & Draine 2001b). Depletion measurements provide important limits on the elemental abundance locked in dust grains (e.g., Jenkins 2009; Tchernyshyov et al. 2015). Experimentally, many studies rely on material thought to be ISM dust analogs to provide laboratory constraints on optical properties and heat capacities (e.g., Richey et al. 2013; Demyk et al. 2017; Mutschke & Mohr 2019).

Both physical and modified blackbody models are almost always calibrated in the Milky Way (MW), where the relevant observables of dust are well constrained. This includes measurements of the diffuse emission and extinction per H

column of the ISM at high Galactic latitudes also referred to as the Milky Way cirrus (e.g., Compiègne et al. 2011; Guillet et al. 2018). The cirrus is also a unique place where the interstellar radiation field that heats dust grains, a necessary component to constrain models, can be estimated. The radiation field measured by Mathis et al. (1983) at the galactocentric distance $D_G = 10$ kpc is generally used to describe the starlight heating dust grains.

The stringency with which each model follows the elemental abundances locked in dust grains from depletion studies varies. Some models use them as strict constraints (e.g., Gordon et al. 2014). On the other hand, most physical models allow more flexibility in the mass of metals locked up in dust grains, to more closely match other, better-constrained observables. For example, the Zubko et al. (2004) dust models follow the depletion constraints strictly, while the Weingartner & Draine (2001b) ones can require up to ∼30% (assuming Si/H = 36 ppm in the model) more silicon than observed in the cold neutral medium. However, the latter models reproduce the observed extinction to a better degree than the former.

With the increasing number of observational constraints on dust models, the complexity of physical dust models has grown. One of the earliest dust models described grains as a single mixture with a power-law size distribution (Mathis et al. 1977). Later on, very small grains known as polycyclic aromatic hydrocarbons (PAHs) were suggested to be responsible for the mid-IR emission features (Leger & Puget 1984; Allamandola et al. 1985) and included in dust models. While some dust models consider them to be defined by their size (in the model description; e.g., Draine & Li 2007; Compiègne et al. 2011; Galliano et al. 2011), other models identify the mid-IR feature carriers in the form of aromatic-rich mantles onto amorphous grains (e.g., Jones et al. 2013 and their hydrogenated amorphous hydrocarbon (HAC) component).

The precise nature of large grains is also uncertain. The presence of amorphous silicate material in grains was demonstrated early on by conspicuous absorption features (Mathis et al. 1977; Kemper et al. 2004) and included in dust models. But their exact composition remains an active research topic (e.g., Zeegers et al. 2019). While some models have a strong focus toward reproducing the observations (e.g., Draine & Li 2007, "astrosilicates"), other models are closely tied to new laboratory data (e.g., Jones et al. 2013, olivine and pyroxene). Finally, with the growing amount of far-IR polarization data, new models have emerged and take into account this important grain property (e.g Guillet et al. 2018; B. S. Hensley & B. T. Draine 2021, in preparation, hereafter HD21). Future missions and instruments are being developed to focus on polarization and will bring new constraints to dust properties (e.g., SOFIA/HAWC+: Harper et al. 2018).

There are now several physical dust models available, which are all different in some—sometimes small—ways. However, these small differences in modeling can lead to significant differences in the derived dust properties, as many studies have shown in nearby galaxies. For instance, Gordon et al. (2014) and Chiang et al. (2018) have used a number of blackbody variations (e.g., simple power-law emissivity, two temperatures, broken-emissivity) to model the far-IR SEDs of the Magellanic Clouds and M101, respectively. They both found that the dust mass derived by several blackbody variations (namely, simple power-law emissivity, two temperature) violates the available elemental content, making these

approaches unlikely to be valid descriptions of dust grain emission. In the Magellanic Clouds, Chastenet et al. (2017) found that dust masses can vary by almost an order of magnitude depending on the physical model chosen. In the Large Magellanic Cloud, Paradis et al. (2019) found that not all models require both neutral and ionized PAHs for a good fit at short wavelengths.

Other discrepancies may arise from simply using a different fitting approach, where uncertainties are treated differently, or with a different data set. For instance, Sandstrom et al. (2010) found an increased abundance of PAHs in dense gas regions of the Small Magellanic Clouds. This behavior was confirmed, but with different PAH fractions in Chastenet et al. (2019), by using the same model with a different wavelength sampling. Most of the uncertainties in comparing the results of the studies mentioned above arise from the wavelength coverage of their data set, the definition of radiation field(s) they use, or simply the dust model they choose.

To reach coherent results on dust properties (dust-to-gas ratio, dust-to-metal ratio, fraction of PAHs, etc.), we need to be able to compare between model results. In this paper, we carry out a rigorous comparison among some of the widely used dust models available in the literature by fitting the IR emission of M101 (NGC 5457) in a strictly identical way for all models. We therefore reduce the differences to those due to the physical modeling choices only. We compare the models from Compiègne et al. (2011), Draine & Li (2007), and The Heterogeneous dust Evolution Model for Interstellar Solids (THEMIS; overview in Jones et al. 2017), as well as HD21. We also include two modified blackbody models previously used in the literature: a simple-emissivity and a broken-emissivity modified blackbody.

We perform our analysis on the galaxy M101 (NGC 5457), which has multiple advantages. First, its distance (∼6.7 Mpc; Tully et al. 2009) and low inclination allow for well-resolved photometry, even in the far-IR. Second, the available IR photometry and spectroscopy from recent space telescopes with high sensitivity are ideal to constrain the dust models. Finally, the metallicity gradients of M101 also offer an independent route to put an upper limit on its dust content. The galaxy has detailed measurements of metallicity from auroral lines (e.g., Croxall et al. 2016; Berg et al. 2020), which put good constraints on the gas-phase metal abundance. It has also been extensively targeted for deep H I and CO observations (Walter et al. 2008; Leroy et al. 2009), allowing us to account for all the gas (modulo any limitations in the ability of the CO and 21 cm lines to trace the gas). Combining these, we can evaluate the impact of model choice on derived dust properties across a wide range of environments with well-understood metal and gas content.

In Section 2, we present the photometry used to sample the IR emission of M101. Section 3 describes the physical and modified blackbody dust models and Section 3.3.4 the technical aspects of the emission fitting technique. The results of these fits are presented in Section 5 with discussions of the differences in dust properties yielded by the dust models. Finally, in Section 6, we analyze the calibration differences in the dust models themselves.

2. Data

We present our adopted distance and orientation parameters for M101 in Table 1.

Table 1
M101 (NGC 5457) Properties

Property	Value	Reference
R.A.	14:03:12.6	Makarov et al. (2014)[a]
Decl.	+54:20:57	Makarov et al. (2014)[a]
Inclination	30°	de Blok et al. (2008)[b]
Position angle	38°	Sofue et al. (1999)
r_{25}	11′.4	Makarov et al. (2014)[a]
Distance	6.7 Mpc	Tully et al. (2009)

Notes.
[a] From the HyperLEDA database, http://leda.univ-lyon1.fr/.
[b] Note the difference from the HyperLEDA database value (16°).

In order to derive the dust properties in M101, we perform fits to its IR SED, composed of measurements at 16 different photometric bands:

1. 3.4, 4.6, 12, and 22 μm from the Wide-field Infrared Survey Explorer (WISE; Wright et al. 2010). We use the maps delivered by Leroy et al. (2019) in the $z = 0$ Multiwavelength Galaxy Survey, already convolved to a 15″ FWHM Gaussian resolution;

2. 3.6, 4.5, 5.8, and 8.0 μm from the Infrared Array Camera instrument (IRAC; Fazio et al. 2004), and 24 and 70 μm from the Multiband Imaging Photometer for Spitzer instrument (MIPS; Rieke et al. 2004),[8] both on board the Spitzer Space Telescope (Werner et al. 2004). We used the product delivery DR5[9] from the Local Volume Legacy survey for the IRAC and MIPS maps (Dale et al. 2009);

3. 70, 100, and 160 μm from the Photoconductor Array Camera and Spectrometer instrument (PACS; Poglitsch et al. 2010) and 250, 350, and 500 μm from the Spectral and Photometric Imaging Receiver instrument (SPIRE; Griffin et al. 2010), both on board the Herschel Space Observatory (Pilbratt et al. 2010). We downloaded the scans from the KINGFISH program (Kennicutt et al. 2011) in the Herschel Science Archive and processed them from L0 to L1 with HIPE (v. 15; PACS Calibration v. 77; SPIRE Calibration v. 14.3; Ott 2010) and Scanamorphos (v. 25; Roussel 2013).

2.1. Data Processing

We correct the images for extended-source calibration appropriately and convert them to the same units in the following way. We apply extended-source correction factors for the IRAC images. These are multiplicative corrections of 0.91, 0.94, 0.695, and 0.74 at 3.6, 4.5, 5.8, and 8.0 μm, respectively, as suggested by the IRAC Instrument Handbook.[10] For SPIRE, we adopt calibration factors of 90.646, 51.181, and 23.580 MJy/sr/(Jy/beam) at 250, 350, and 500 μm, respectively, as suggested by the SPIRE Handbook.[11]

---

[8] We do not use MIPS 160 (e.g., as opposed to Aniano et al. 2020) to gain back some resolution (MIPS 160 PSF is ~39″) without losing wavelength coverage. This does not lead to major differences.
[9] https://irsa.ipac.caltech.edu/data/SPITZER/LVL/LVL_DR5_v5.pdf
[10] https://irsa.ipac.caltech.edu/data/SPITZER/docs/irac/iracinstrumenthandbook/29/
[11] http://herschel.esac.esa.int/Docs/SPIRE/spire_handbook.pdf

Table 2
Band-related Details

Band	σ_{bkg}[a] 10^{-1} MJy sr^{-1}	m_{cal}[b] %	m_{sta}[c] %
WISE 3.4	0.170	2.4	10.0
IRAC 3.6	0.149	9.0	1.5
IRAC 4.5	0.107	6.0	1.5
WISE 4.6	0.095	2.8	10.0
IRAC 5.8	0.109	30	1.5
IRAC 8.0	0.085	26	1.5
WISE 12	0.114	4.5	10.0
WISE 22	0.055	5.7	10.0
MIPS 24	0.049	4.0	0.4
MIPS 70	5.24	10.0	4.5
PACS 70	10.7	10.0	2.0
PACS 100	10.1	10.0	2.0
PACS 160	7.95	10.0	2.0
SPIRE 250	3.96	8.0	1.5
SPIRE 350	2.73	8.0	1.5
SPIRE 500	1.82	8.0	1.5

Notes. References to the σ_{cal} and σ_{sta} Coefficients—WISE: http://wise2.ipac.caltech.edu/docs/release/prelim/expsup/sec4_3g.html; IRAC: Reach et al. (2005) and https://irsa.ipac.caltech.edu/data/SPITZER/docs/irac/iracinstrumenthandbook/29/; MIPS: Engelbracht et al. (2007) and Gordon et al. (2007); PACS: Müller et al. (2011) and Balog et al. (2013); SPIRE: Griffin et al. (2010) and Bendo et al. (2013).
[a] The background standard deviation in the pixels considered to measure the background covariance matrix, once the maps are background-removed, convolved, and projected.
[b] m_{cal} is the error on the calibration used in each instrument. The large errors of the IRAC bands are from the extended-source corrections, which we consider to be correlated calibration errors.
[c] m_{sta} measures the stability of an instrument, i.e., the scatter when measuring the same signal.

These factors convert the data to MJy sr^{-1} from Jy/beam and also correct from point-source to extended-source calibration. The PACS data in units of Jy/pixel are converted to units of MJy sr^{-1} using the image pixel size (contained in the headers).

We then process all of the maps following the same steps, as described below. We remove a background in each image at their native resolution by fitting a 2D plane using regions identified not to have significant galaxy emission. We find these regions with the following procedure: (1) we use the r_{25} radius ($r_{25} \sim 12'$) to first mask the galaxy (this covers the visible SPIRE 500 emission completely); (2) we measure the median of the remaining pixels and the standard deviation, and clip all of those that are three standard deviations above that median; (3) we iterate that clipping until the medians at iterations i and $i + 1$ differ by less than 1%. This clipping is only done for the purpose of measuring a background level, and we do not keep this mask applied to the data for the following steps. Table 2 lists the final standard deviations of the background pixels in each band.

Each map is then convolved to the SPIRE 500 PSF (FWHM $\sim 36''$) using convolution kernels from Aniano et al. (2011). Finally, all of the maps are aligned and projected onto the astrometric grid of the SPIRE 500 image. In Figure 1, we show the 16 bands that we use to model the dust emission from 3.4 to 500 μm.

The final pixel size (9″) oversamples the SPIRE 500 beam size, to which all data are convolved. We take this into account
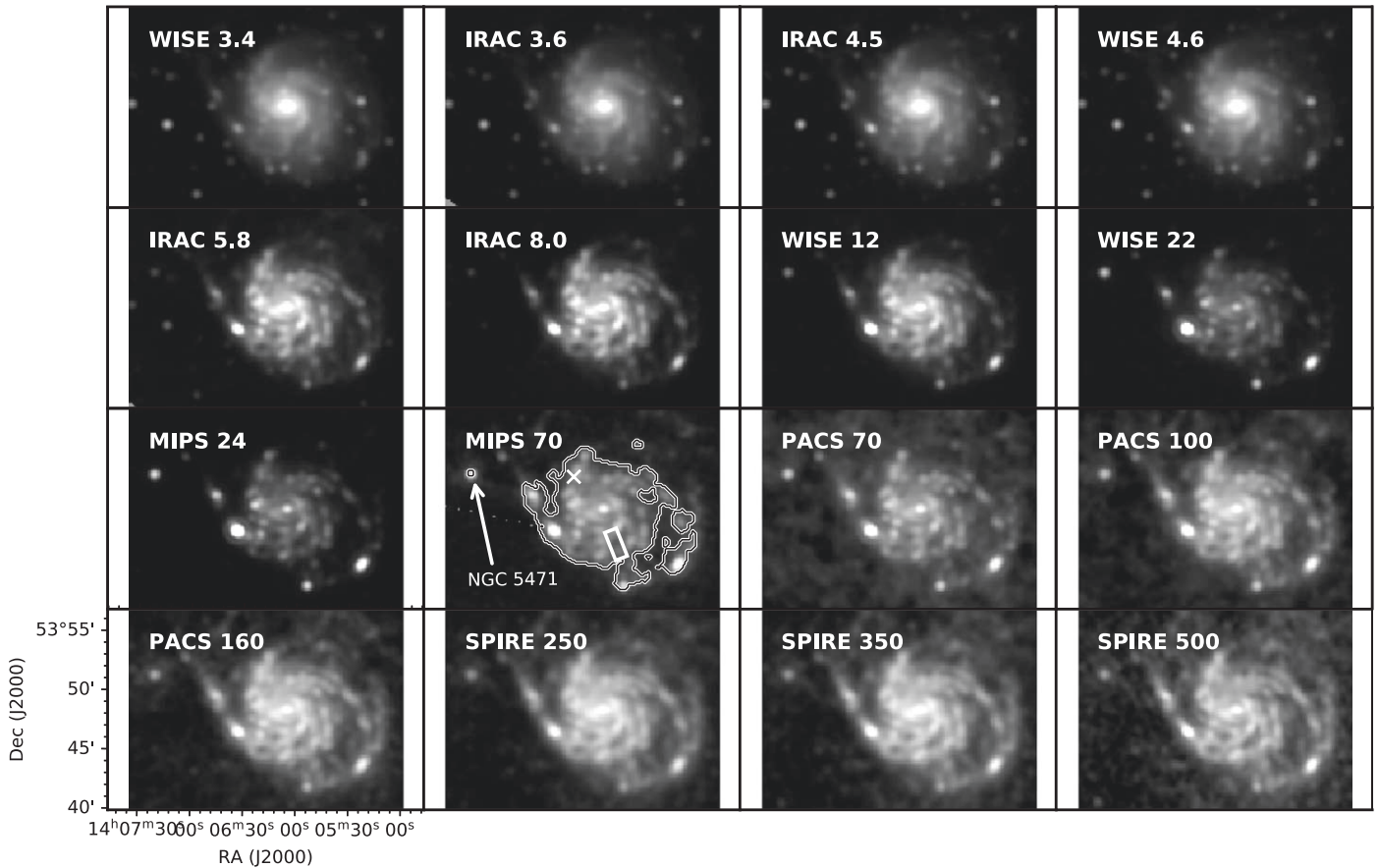
Figure 1. Emission of M101 (NGC 5457) from 3.4 to 500 μm, in all of the bands used in this study. The maps show the final version of each map: after extended-source correction (IRAC and SPIRE bands), unit conversion (PACS and SPIRE bands), background removal, convolution to SPIRE 500 PSF ($\sim$36''), and regridding. On the MIPS 70 panel, we also show the location of the pixel for the fit example (white cross; Figure 4), the region used for the IRS measurement (white rectangle; Section 5.6), and the contours for the 3σ detection threshold.

by correcting by $\sqrt{N_{\mathrm{pix}}/N_{\mathrm{beam}}}$ when calculating uncertainties on quantities that use the values of multiple pixels.

2.2. Ancillary Data: Neutral and Molecular Gas

In Section 6, we use gas surface density and metallicity measurements in addition to IR SEDs. We use the same data as Chiang et al. (2018) to get the total gas surface density, Σ_{gas}, combining gas surface density maps from H I 21 cm and CO(2 → 1) emission converted to H$_2$. The H I 21 cm line data is from the THINGS collaboration (The H I Nearby Galaxy Survey; Walter et al. 2008). The map is converted from integrated intensity to surface density assuming optically thin 21 cm emission, following Walter et al. (2008, Equations 1 and 5, and multiplying by the atomic mass of hydrogen).

We use CO (2 → 1) emission from HERACLES (Leroy et al. 2009) and convert it to H$_2$ surface density, assuming a line ratio $R_{21} = 0.7$ and a α_{CO} conversion factor, in units of $M_\odot/\mathrm{pc}^2$ (K km s^{-1})$^{-1}$, following two prescriptions (both including helium): the first one is representative of the MW CO-to-H$_2$ conversion,[12]

$$\alpha_{\mathrm{CO}}^{\mathrm{MW}} = 4.35, \qquad (1)$$

and the second one follows Bolatto et al. (2013),

$$\alpha_{\mathrm{CO}}^{\mathrm{BWL13}} = 2.9 \, e^{(0.4/Z')} (\Sigma_{\mathrm{Total}}^{100})^{-\gamma}$$
$$\mathrm{with} \begin{cases} \gamma = 0.5 & \text{if } \Sigma_{\mathrm{Total}}^{100} \geqslant 1, \\ \gamma = 0 & \text{otherwise} \end{cases}, \qquad (2)$$

where Z' is the metallicity relative to solar metallicity,[13] $\Sigma_{\mathrm{Total}}^{100}$ is the total surface density map in units of $100 \, M_\odot \, \mathrm{pc}^{-2}$. The gas maps are convolved to a 41'' Gaussian PSF (Chiang et al. 2021); because we plot the radial profile of the gas maps by averaging in growing annuli, we find that the minor differences between the dust and gas maps resolutions are negligible. We measure an uncertainty of $\sim$0.3 K km s^{-1} for the CO(2 → 1) map and an uncertainty of $\sim$0.4 $M_\odot \, \mathrm{pc}^{-2}$ for the H I 21 cm map.[14] We build a radial profile by averaging Σ_{gas} in growing annuli from the center out to r_{25}.

2.3. Ancillary Data: Metallicity

Metallicity measurements $12 + \log_{10}(\mathrm{O/H})$ are taken from the CHAOS survey (Berg et al. 2020), derived from 72 H II regions of M101. In particular, we use their

---

[12] A standard $X_{\mathrm{CO}} = 2 \times 10^{20}$ (K km s^{-1})$^{-1}$ is assumed for the column density conversion factor. The mass of helium and heavier elements have been accounted for in α_{CO}.

[13] $Z' = 10^{((12+\log(\mathrm{O/H}))-(12+\log(\mathrm{O/H})_\odot))}$ with $12 + \log(\mathrm{O/H})_\odot = 8.69$.
[14] The rms per channel is $\sim$0.46 mJy/beam. Assuming $\sigma_{z,\,\mathrm{gas}} = 11$ km s^{-1} (Leroy et al. 2008), the uncertainty is 0.96 $M_\odot \, \mathrm{pc}^{-2}$. The 5% calibration error (Walter et al. 2008) becomes significant in the dense regions.

Table 3
Fitting Parameters

Parameter	Range	Step	Unit
All physical models			
$\log_{10}(\Sigma_{\rm dust})$	[−2.2, 0.1]	0.035	$M_\odot\,{\rm pc}^{-2}$
$U_{\rm min}$	[0.1, 50]	Irr[a]	⋯
$\log_{10}(\gamma)$	[−4, 0]	0.15	⋯
$\log_{10}(\Omega_*)$	[−1, 2.5]	0.075	⋯
Model-specific			
DL07, HD21: $q_{\rm PAH}$	[0, 6.1]	0.25	%
THEMIS: $f_{\rm sCM20}$[b]	[0, 0.5]	0.03	⋯
MC11: $f_{\rm PAHs}$[b]	[0, 0.5]	0.03	⋯
Modified blackbody models			
$\log_{10}(\Sigma_{\rm dust})$	[−2.2, 0.1]	0.035	$M_\odot\,{\rm pc}^{-2}$
$T_{\rm dust}$	[12, 35]	0.3	K
SE: β, BE: β_2	[−1,4]	0.05	⋯

Notes.
[a] $U_{\rm min} \in \{0.1, 0.12, 0.15, 0.17, 0.2, 0.25, 0.3, 0.35, 0.4, 0.5, 0.6, 0.7, 0.8, 1.0, 1.2, 1.5, 1.7, 2.0, 2.5, 3.0, 3.5, 4.0, 5.0, 6.0, 7.0, 8.0, 10.0, 12.0, 15.0, 17.0, 20.0, 25.0, 30.0, 35.0, 40.0, 50.0\}$.
[b] We use a "fraction" parameter so that $\Sigma_X = f_X \times \Sigma_d$, where $X = \{{\rm sCM20}^{\rm THEMIS}, {\rm PAHs}^{\rm MC11}\}$.

fitted metallicity gradient

$$12 + \log_{10}({\rm O/H}) = 8.78 \pm 0.04 - 0.75 \pm 0.07\,(r/r_{25}) \quad (3)$$

to convert it to a radial profile of metal surface density (see Section 6.1). We adjusted the slope given by Berg et al. (2020, 0.90) to account for the different r_{25} used here. Berg et al. (2020) find that the scatter in individual region metallicities around the measured gradient is ∼10%.

Tracing the total metal mass from nebular emission lines of oxygen is subject to systematic uncertainties. As pointed out by Jenkins (2009), oxygen shows unexplained depletion patterns, compared to how much is expected to be locked in the solid phase. However, Peimbert & Peimbert (2010) measured the depletions of heavy elements in Galactic and extragalactic H II regions and found minimal depletion of oxygen (≲0.1 dex). Other elements may be of use for tracing metallicity (as is the case in Berg et al. 2020), but given the widespread use of O/H for extragalactic studies, we use the typical $12 + \log({\rm O/H})$ tracer.

3. Dust Emission Models

The goal of this study is to investigate the differences in dust properties derived using physical and modified blackbody models. In this section, we present the characteristics of each model. The parameters we use to fit the IR SEDs are presented in Table 3. A summary table of the following information is presented in Appendix A.

3.1. Modified Blackbodies

We use single-temperature modified blackbody models. For these two models, we only fit photometry from 100 to 500 μm. At $\lambda < 100\,\mu$m, stochastically heated grains contribute to the emission and are not well modeled by a modified blackbody. Assuming the optically thin case, the dust emission I_ν is described as

$$I_\nu(\lambda) = \kappa_\nu(\lambda)\,\Sigma_{\rm dust}\,B_\nu(\lambda, T_{\rm dust}), \quad (4)$$

where $B_\nu(\lambda, T_{\rm dust})$ is the Planck function at wavelength λ (in MJy sr^{-1}), $T_{\rm dust}$ the dust temperature, $\Sigma_{\rm dust}$ the dust surface density, and κ_ν the opacity. We use the simple power-law opacity (Equation (5)) and a broken power-law opacity (Equation (6)), which we normalize at $\lambda = 160\,\mu$m. The broken power-law model presented the best results in terms of quality of fits in the study by Chiang et al. (2018) and yielded physically reasonable $\Sigma_{\rm dust}$ and $T_{\rm dust}$ values in their study.

We follow Gordon et al. (2014) and Chiang et al. (2018) and calibrate the opacity values for each model. We fit the modified blackbody model to the dust emission per H column of the MW high-latitude cirrus described in Chiang et al. (2018) to derive the opacity. The abundance constraints are based on a depletion strength factor typical for lines of sight with $N_{\rm H}$ similar to that of the MW cirrus, e.g., $F_* = 0.36$ (Jenkins 2009). This sets the allowed dust mass per H atom. By fitting the temperature for the MW cirrus, we can then derive the opacity for each modified blackbody model. More details on the opacity and comparison to the physical models can be found in Section 3.2.

3.1.1. Simple Emissivity

In this case, the opacity is described as a single power law:

$$\kappa_\nu = \kappa_{\nu_0}\left(\frac{\nu}{\nu_0}\right)^\beta, \quad (5)$$

where β is the spectral index. For all blackbody models, we fix $\lambda_0 = 160\,\mu$m and $\nu_0 = c/\lambda_0$. The free parameters for this model are then the dust surface density $\Sigma_{\rm dust}$, the dust temperature $T_{\rm dust}$, and the dust spectral index β. In this model, the calibrated $\kappa_{\nu_0} = 10.10 \pm 1.42\,{\rm cm}^2\,{\rm g}^{-1}$ (Chiang et al. 2018) from fitting the high-latitude cirrus as described above.

3.1.2. Broken Emissivity

The broken-emissivity model stemmed from the identification of the submillimeter excess (Gordon et al. 2014). It allows a change of the dust spectral index with wavelength, meant to better reproduce the far-IR slope than does a simple modified blackbody. In this model, the value of the opacity is wavelength dependent, such that

$$\kappa_\nu = \begin{cases} \kappa_{\nu_0}\left(\dfrac{\nu}{\nu_0}\right)^\beta & \lambda < \lambda_c \\[2ex] \kappa_{\nu_0}\left(\dfrac{\nu_c}{\nu_0}\right)^\beta\left(\dfrac{\nu}{\nu_c}\right)^{\beta_2} & \lambda \geqslant \lambda_c \end{cases}, \quad (6)$$

where λ_c is the wavelength at which the opacity changes and ν_c its equivalent frequency. Following Chiang et al. (2018), we fix $\beta = 2$ and $\lambda_c = 300\,\mu$m. The free parameters are then the dust surface density $\Sigma_{\rm dust}$, the dust temperature $T_{\rm dust}$, and the second dust spectral index β_2. The calibrated opacity, κ_{ν_0}, for this model is $20.73 \pm 0.97\,{\rm cm}^2\,{\rm g}^{-1}$ (Chiang et al. 2018), as described above.

3.2. Opacity Calibrations

The physical dust models used in our study have opacities that are set by each individual model calibration procedure. All models use similar constraints from the MW high-latitude cirrus (described in more detail in Appendix A). For ease of comparison to the opacities we have derived for the modified blackbody models ($10.1 \, \mathrm{cm^2 \, g^{-1}}$ for the simple-emissivity and $20.7 \, \mathrm{cm^2 \, g^{-1}}$ for the broken-emissivity model at 160 μm), we list the opacity in the physical models below all scaled to 160 μm for comparison:

1. Draine & Li (2007): from the Weingartner & Draine (2001b) model updated in DL07, we report $\kappa_{160} = 10.2 \, \mathrm{cm^2 \, g^{-1}}$ (see also Bianchi 2013);
2. Compiègne et al. (2011): from the work of Bianchi (2013), we report $\kappa_{160} = 12.0 \, \mathrm{cm^2 \, g^{-1}}$;
3. Jones et al. (2017, THEMIS): from the work of Galliano et al. (2018), we report $\kappa_{160} = 14.2 \, \mathrm{cm^2 \, g^{-1}}$;
4. HD21: the models use $\kappa_{160} \sim 9.95 \, \mathrm{cm^2 \, g^{-1}}$ (B. Hensley 2021, private communication).

For all models, we use the listed opacity regardless of the specific environment in M101 we are studying. Few of the currently available physical dust models have been calibrated in any environment other than the MW cirrus (although the Draine & Li 2007 model does have Small and Large Magellanic Cloud–like calibrations, though they are not widely used even for these very galaxies; Sandstrom et al. 2010; Chastenet et al. 2019). Indeed, it is standard in current extragalactic applications to apply MW cirrus $R_V = 3.1$ dust calibrations across all environments (e.g., Davies et al. 2017; Aniano et al. 2020). In detail, this is unlikely to be correct because the opacity can and probably should evolve as a function of the environment, and it is clear that a single $F_* = 0.36$ value does not describe the depletion in the ISM over the full range of column densities probed in galaxies. However, for the purposes of our comparative study of widely used dust models, we proceed by using the $R_V = 3.1$ MW cirrus calibrations from each model. Even if there were a potential way to adjust opacity with the H column in M101, work by Ysard et al. (2015) using THEMIS suggests that this is insufficient to predict changes in dust properties.

3.3. Physical Dust Models

Physical dust models assume a composition, density, and shape for the dust grains and adopt heat capacities and optical properties from laboratory and theoretical studies that are appropriate for such materials. For simplicity, most models assume spherical grains or planar molecules for PAHs. In the case of PAHs, the grains/molecules are additionally described by an ionization state, which changes the absorption cross-sections as a function of wavelength. The temperature and emission of a grain of a given size, shape, and composition in a radiation field with a specified intensity and spectrum can then be calculated analytically (e.g., Draine & Lee 1984; Desert et al. 1986).

The full dust population is represented by a grain size distribution and abundance relative to H for the specified compositions. Physical dust models are calibrated by adjusting the grain size distributions and dust mass per H to simultaneously match observations of extinction, emission, and abundances (and more recently, polarization) in a location

where the underlying radiation field that is heating the dust is well known. This has generally been taken to be the high-latitude MW cirrus, where the radiation field intensity and spectrum are approximately given by the Mathis et al. (1983) model for the solar neighborhood. The degree to which the models must adhere to the somewhat uncertain abundance constraints varies from model to model. For example, the modified blackbody models from Gordon et al. (2014) use the depletion measurements in the MW as a strict limit. However, most physical models allow the final element abundances to vary from depletions, using them only as a loose guide.

In the following, we use four physical dust models: Draine & Li (2007), Compiègne et al. (2011), THEMIS (Jones et al. 2017), and HD21. Here we briefly describe these models, the key differences between them. Details on their respective calibration methodologies can be found in Appendix A.

3.3.1. Draine & Li (2007)

In the Draine & Li (2007, hereafter DL07) model, dust is composed of PAHs, graphite grains, and amorphous silicate grains. It stems from the original models presented in Li & Draine (2001). The carbonaceous dust optical properties are adopted from Li & Draine (2001) with updates to the PAH cross sections and form of the grain size distribution. A balance between ionized and neutral PAHs is assumed, following Li & Draine (2001). The optical properties of silicate material are adopted from the "astrosilicates" in the original model. We do not make use of the mass renormalization in Draine et al. (2014).

The mass fraction of PAHs, q_{PAH}, is described as the mass of carbonaceous grains with less than 10^3 carbon atoms with respect to total dust mass. We effectively obtain q_{PAH} in percent by converting the parts-per-million carbon abundance b_{C} to a PAH fraction, using the reference $q_{\mathrm{PAH}} = 4.7\% \equiv b_{\mathrm{C}} = 55$ ppm.

The calibration of the model is described in several papers (Draine & Li 2001; Li & Draine 2001; Weingartner & Draine 2001b). We use the DL07 MW model, with $R_V = 3.1$, which has a fixed ratio of silicate to carbonaceous grains. Details on the calibration can be found in Appendix A.1.

3.3.2. Compiègne et al. (2011)

The Compiègne et al. (2011, hereafter MC11) model is composed of PAHs, hydrogenated amorphous carbon grains, and amorphous silicate grains. The size distribution of the carbonaceous components includes PAHs, small amorphous carbon grains (SamC), and large amorphous carbon grains (LamC). The PAH cross sections and ionization as a function of size adopted in the model are based on Draine & Li (2007) with slight modifications to the cross sections of several bands. Amorphous carbonaceous grains have optical properties from Zubko et al. (2004) and heat capacities from Draine & Li (2001). The amorphous silicates (aSil) have optical properties from Draine (2003) and heat capacities from Draine & Li (2001). Details on the calibration can be found in Appendix A.2.

The DustEM [15] tool allows both ionized and neutral PAHs to be fit independently. Because not all models allow that

---

[15] DustEM is a tool that outputs extinction, emission, and polarization of dust grains heated by a given radiation field. See details at https://www.ias.u-psud.fr/DUSTEM/.

separation, we tie their emission spectra together by summing them, hence keeping their ratio constant at roughly 60% neutral and 40% ionized.[16] Additionally, we fix the mass fractions of the large-carbonaceous-to-silicate grains such as $(M_{dust}^{LamC}/M_H)/(M_{dust}^{aSil}/M_H) = 0.22$.[17] Because these share a very similar far-IR spectral index, their respective emission cannot be properly determined independently with our wavelength coverage and would lead to degenerate abundances if fit separately.

3.3.3. THEMIS

THEMIS (Jones et al. 2013; Köhler et al. 2014; Ysard et al. 2015; Jones et al. 2017) is a core/mantle dust model, consisting of large silicate and hydrocarbons, both coated with aromatic-rich particles (HACs). This model defines its dust components by focusing strongly on laboratory data, slightly adjusted to better match observations. We use the diffuse ISM version of the model, described in Jones et al. (2013). The amorphous carbon grain properties are size dependent, and there is no strictly independent population of grains responsible for the mid-IR features, carried by aromatic clusters in the form of mantles and very small grains (sCM20). As they grow to larger grains (lCM20) in size, their core becomes aliphatic rich, coated with an aromatic mantle. The silicate grains (aSilM5) in particular are discussed in Köhler et al. (2014). They are a mixture of olivine and pyroxene-type material, with nanoinclusions of Fe and FeS. Their mass ratio is kept constant due to their extreme resemblance in emission in the considered wavelength range. The dust evolution models (from diffuse to denser medium) are discussed in Ysard et al. (2015), with the impact of aggregates and thicker mantles on the final abundances. In the diffuse model we use, aSil has a 5 nm mantle, and hydrocarbons have a 20 nm mantle. In our fitting, the lCM20-to-aSilM5 mass ratio is kept constant, such as $(M_{dust}^{lCM20}/M_H)/(M_{dust}^{aSilM5}/M_H) = 0.24$.[18] Details on the calibration can be found in Appendix A.3.

3.3.4. B. S. Hensley & B. T. Draine (2021, in preparation)

Rather than employ separate amorphous silicate and carbonaceous grain components, the (HD21) model invokes a single homogeneous composition, "astrodust" (Draine & Hensley 2021), to model most of the interstellar grain mass. In addition to astrodust, the model incorporates PAHs using the cross sections from Draine & Li (2007) and a small amount of graphite using the turbostratic graphite model presented in Draine (2016). The HD21 model was developed to reproduce the observed properties of dust polarization, including both polarized extinction and emission, in addition to total extinction and emission. This results in the raising of the emissivity in the far-IR, forcing the dust to be slightly cooler than other models, and requiring a higher radiation field to get comparable amounts of emission. We use cross sections computed for 2:1 prolate spheroids, but the grain shape has only a small effect on the far-infrared total intensity studied in this work. Details on the calibration can be found in Appendix A.4.

For the purposes of this study, the HD21 model has been parameterized in the same way as Draine & Li (2007), i.e., utilizing parameters U and q_{PAH}.

4. Fitting Methodology

4.1. Making Matched Model Grids

Because each model was developed independently, it is not always possible to create model grids that have exactly the same parameter sampling, because of the lack of parameter equivalence. However, we attempt to do so as much as possible.

Radiation field—We implement identical dust heating in each of the physical models: a fraction γ of the dust mass in a pixel is heated by a power-law distribution of radiation fields with $U_{min} < U \leqslant U_{max}$ (Dale et al. 2001), where U is the interstellar radiation field, expressed in units of the MW diffuse radiation field at 10 kpc from Mathis et al. (1983). The remaining fraction of dust $(1 - \gamma)$ is heated by the minimum radiation field U_{min} (Draine & Li 2007):

$$\frac{1}{M_{dust}} \frac{dM_{dust}}{dU} = (1 - \gamma) \, U_{min}$$
$$+ \gamma \, \frac{(\alpha - 1)}{U_{min}^{1-\alpha} - U_{max}^{1-\alpha}} \, U^{-\alpha}. \tag{7}$$

We fix $\alpha = 2$ for all models; $U_{max} = 10^7$ for the DL07, THEMIS, and MC11 models; and $U_{max} = 10^6$ for HD21. This choice is constrained by the available parameter ranges in the models: the U_{max} values for the DL07 and HD21 models are fixed, and we do not have the freedom to change them; thanks to DustEM, we can adjust U_{max} for MC11 and THEMIS.[19] For THEMIS and the MC11 model, which have multiple dust populations that can be independently heated, each population is heated by the same radiation field.

The minimum radiation field parameter grid is fixed by the values provided in the Draine & Li (2007) model. Thanks to the DustEM tool, we can use the exact same values with THEMIS and the MC11 model. These parameter values in HD21 however are not exactly identical to those in U_{min}^{DL07}. We therefore use the spectra with the closest U_{min}^{HD21} values. Although not strictly equal, the radiation field values in Hensley & Draine are within 5% of U_{min}^{DL07}.

For the modified blackbody models, we use a single radiation field intensity and translate it into a dust temperature. We use the relationship

$$U \propto T_{dust}^{\beta+4} \quad \text{with } \beta = 2 \tag{8}$$

to convert U_{min} to T_{dust} and find the approximately matching sampling to use in the blackbody models. We use the normalization from Draine et al. (2014), i.e., $U = 1$ at $T_{dust} = 18$ K, found using the same radiation field from Mathis et al. (1983).

Mid-IR feature carriers—The q_{PAH} parameter is kept strictly identical between DL07 and HD21. We choose to use THEMIS and the MC11 models in a similar fashion. Despite the definition

---

[16] The ratio of ionized and neutral PAHs is size dependent. The values are set in DustEM from the MIX_PAHx.DAT files.
[17] This value is that from the DustEM file GRAIN_MC10.DAT.
[18] This value is that from the DustEM file GRAIN_J13.DAT.

[19] Using DustEM and THEMIS, we checked the effect of using $U_{max} = 10^6$ or 10^7, for a range of γ values. We find that most of the mid-IR bands used in this study are only minimally affected. The difference for IRAC 4.5 and WISE 4.6 can be significant at $\gamma \geqslant 0.1$, while the maximum γ values reached by the model fits is 0.07 (for DL07). Additionally, these bands are dominated by starlight and mostly modeled by the 5000 K blackbody.
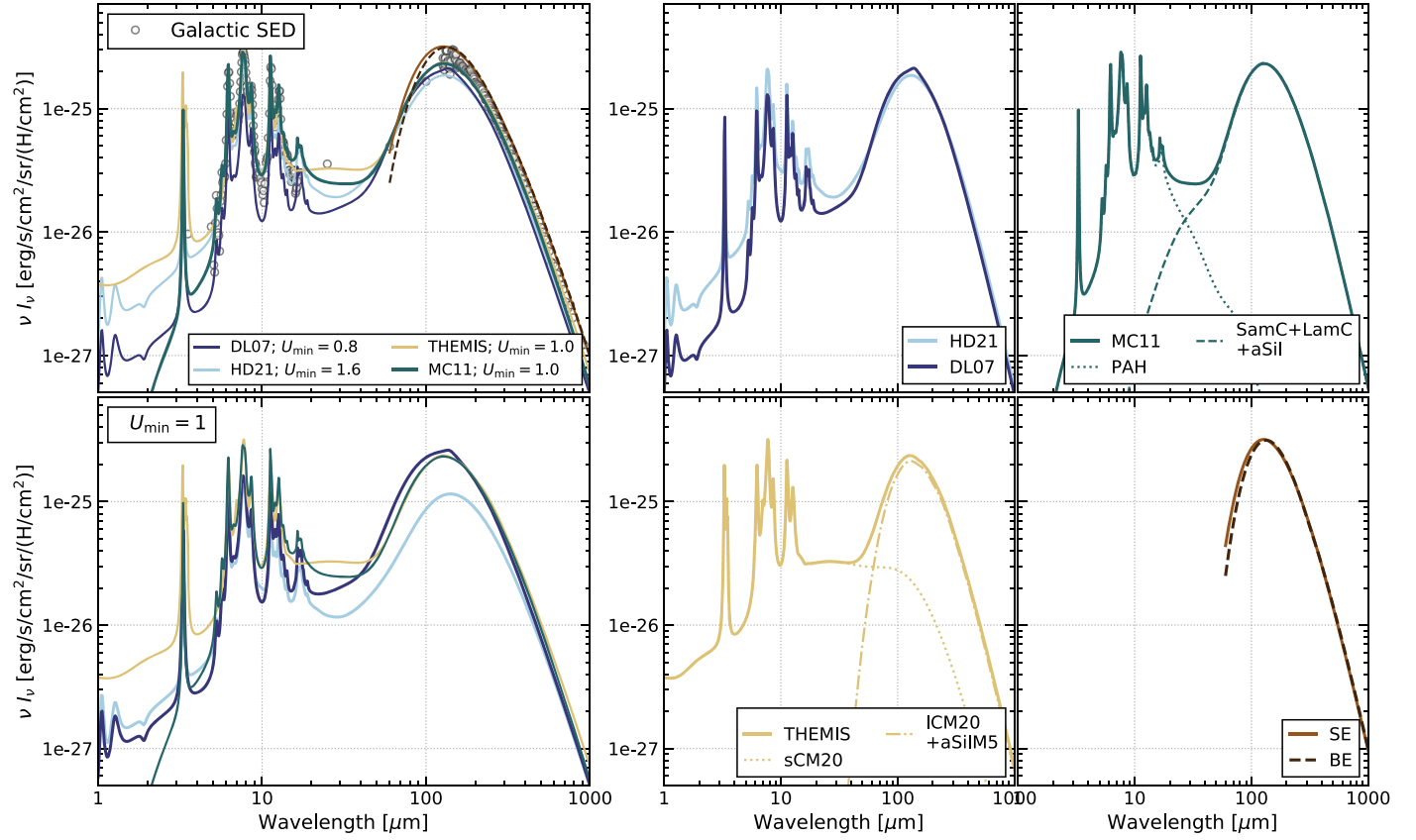
Figure 2. The dust emission models used in this study: Draine & Li (2007), Jones et al. (2017, THEMIS), Compiègne et al. (2011), HD21, simple emissivity, and broken emissivity. Top left: all six models at the U_{min} value that best fits the calibration SED. Bottom left: the four physical models at $U_{min} = 1$. The right side panels show each model at the U_{min} value that best fits the calibration SED and their breakdown as they are used in this study.

of "PAHs" being different in THEMIS, we parameterize the model so that the fraction of small grains can vary, keeping the large-carbonaceous-to-silicate grains ratio constant. The MC11 default model has four populations that can vary independently, and we choose to tie together SamC, LamC, and aSil to leave the amount of PAHs as a free parameter. We explain these choices in more detail in Section 7.

Stellar surface brightness—In addition to the dust model parameters, we use a scaling parameter of a 5000 K blackbody, Ω_*, to model the stellar surface brightness visible at the shortest wavelengths. This temperature is a good approximation as the shortest wavelengths are nearly on the Rayleigh–Jeans tail. The free parameter Ω_* scales the amplitude of the stellar blackbody.

In Table 3, we list the final free parameters we use for each model. There are five free parameters for the physical models, and three for the modified blackbody models. Figure 2 shows all of the dust emission models used in this study. The top-left panel shows the fiducial MW high-galactic-latitude diffuse ISM models, labeled "Galactic SED." The IR MW diffuse emission from Compiègne et al. (2011) is also plotted. The bottom-left panel shows the physical dust models at the same radiation field $U_{min} = 1$. The other different panels detail the models: THEMIS is divided into two grain populations when fitted to the SED of M101 (note that we tie the lCM20 and aSilM5 population); for the MC11 model, we tie the SamC, LamC, and aSil emissions together, and thus there are two free parameters for the dust mass: f_{PAH} or f_{sCM20}, and the total dust surface density. The two modified blackbodies are shown with

their best-fit values to the MW diffuse SED: $\{T_{dust} = 20.9\,\mathrm{K}, \beta = 1.44\}$ for the simple-emissivity model, and $\{T_{dust} = 18.0\,\mathrm{K}, \beta_2 = 1.55\}$ for the broken-emissivity model.

4.2. Fitting Tool

4.2.1. Bayesian Fitting with DustBFF

We use the DustBFF tool from Gordon et al. (2014) to fit the data with the chosen dust models. DustBFF is a Bayesian fitting tool that uses flat priors for all parameters. The probability that a model with parameters θ fits the measurements (S^{obs}) is given by

$$\mathcal{P}(\boldsymbol{S}^{obs}|\theta) = \frac{1}{Q} e^{-\chi^2(\theta)/2}, \qquad (9)$$

with

$$Q^2 = (2\pi)^n \det|\mathbb{C}|$$
$$\chi^2(\theta) = [\boldsymbol{S}^{obs} - \boldsymbol{S}^{mod}(\theta)]^T\ \mathbb{C}^{-1}\ [\boldsymbol{S}^{obs} - \boldsymbol{S}^{mod}(\theta)], \qquad (10)$$

where $\boldsymbol{S}^X$ is the observed ($X = $ obs) or modeled ($X = $ mod) 16 band SEDs used here, and $\mathbb{C}$ is the covariance matrix that includes uncertainties from random noise, astronomical backgrounds, and instrument calibration (described further below).

To create $\boldsymbol{S}^{mod}(\theta)$, each model spectrum is convolved with the spectral responses for the photometric bands used here. PACS and SPIRE band integrations are done in energy units, whereas all the others are done in photon units, as necessitated by the instrument's calibration scheme. We also follow the reference

spectra used for the calibration of each instrument: the MIPS bands require a reference shape in the form of the 10^4 K blackbody while the other bands use a reference shape as $1/\nu$.

4.2.2. Covariance Matrices

The covariance matrix in the previous equations describes the uncertainties on the measured flux, both due to astronomical backgrounds, and instrumental noise and the uncertainties in calibrating the instruments. This takes into account the correlation between the photometric bands due to the calibration scheme and the correlated nature of astronomical background signals. We define a background matrix and an instrument matrix such that $\mathbb{C} = \mathbb{C}_{bkg} + \mathbb{C}_{ins}$ to propagate the correlated errors of the background and noise, and of the calibration uncertainties, respectively.

Background covariance matrix $\mathbb{C}_{bkg}$—The "background" in our images encompasses astronomical signals that do not come from the IR emission of the target M101. It is dominated by different objects depending on the wavelength and can therefore be correlated between bands. For instance, the background from 3.4 to 5.8 μm is mostly from foreground stars, as well as zodiacal light; from 8 to 24 μm, it is from evolved stars and background galaxies; in the far-IR, it is dominated by Galactic cirrus emission and background galaxies. To include this uncertainty, we measure this combination of signals in "background pixels" using the processed data and a masking procedure described in Section 4.2.3.

The elements of the background covariance matrix are calculated as

$$(\mathbb{C}_{bkg})^2_{i,j} = \frac{\sum_k^N (S_i^k - \langle S_i \rangle)(S_j^k - \langle S_j \rangle)}{N - 1}, \quad (11)$$

where S_X^k is the flux of pixel k in band X, and $\langle S_X \rangle$ is the average background emission in band X (close to 0). The final number of 9″ pixels used to measure the covariance matrix is $N = 18{,}920$.

We display the background correlation matrix in Figure 3 (not the elements' absolute values but the Pearson correlation coefficients; see Gordon et al. 2014). Three clear sets of positive correlations appear, as previously explained: correlations are due to starlight in the near-IR, evolved stars and MW cirrus in the mid-IR, and background galaxies and MW cirrus in the far-IR. Additionally, some bands may be noise dominated: it is the case for the PACS 70 band, which is only weakly correlated with other bands.

Instrument calibration matrix $\mathbb{C}_{ins}$—This matrix is calculated as the quadratic sum of the correlated and uncorrelated errors for each instrument. The correlated errors (matrix with diagonal and anti-diagonal terms) refer to the instrument calibration itself (m_{cal} in Table 2, while the uncorrelated errors (matrix with diagonal terms only) express the instrument stability, or repeatability (m_{sta} in Table 2). We use the same calibration errors reported in Chastenet et al. (2017, see Table 2) for the Spitzer /MIPS and Herschel bands. The correlated errors for the IRAC bands were changed to take into account the uncertainties in the extended-source correction factors, larger than the calibration error themselves. The errors due to repeatability are unchanged. The errors for WISE bands were taken from the WISE documentation.[20]
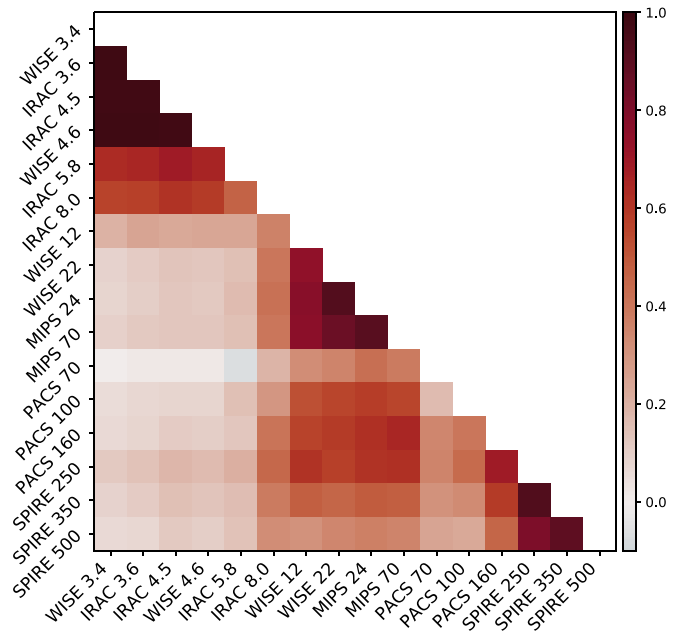
Figure 3. Background correlation matrix. The dark color indicates a strong correlation between the bands. The matrix is symmetric, and we show only half. The text indicates the astronomical signals that dominate the contoured bands and that explain their strong correlation.

The elements of the calibration matrix $\mathbb{C}_{ins}$ are calculated "model by model" as

$$(m_{ins})^2_{i,j} = S_i^{mod}(\theta) \, S_j^{mod}(\theta) \, (m^2_{cal,i,j} + m^2_{sta,i,j}), \quad (12)$$

with particular elements

$m_{cal,i,j} = 0$ if i, j belong to two different instruments;

$m_{sta,i,j} = 0$ if $i \neq j$.

We fit all the pixels that are above 1σ of the background values, in all bands. We use these pixels to show parameter maps and radial profiles, while the galaxy-integrated values are calculated for pixels above 3σ detection above the background (black contours in Appendices B and C).

4.2.3. Stars in the Background/Foreground

Here we describe the masking procedure to measure the background covariance matrix in Section 4.2.2. To do so, we use the final images, i.e., background-subtracted, convolved, and projected to the same pixel grid.

The covariance matrix elements are calculated with the assumption of a Gaussian noise. While the assumption works well for faint and unresolved stars and the cosmic infrared background galaxies, it is no longer correct if we include bright stars. Bright foreground stars only must therefore be cut to measure this matrix. This masking has the effect of making the approximation of Gaussian noise for the remaining background more correct. Note, however, that they are not masked for fitting within the boundary of the galaxy,[21] but only for the purpose of the covariance matrix measurement.

[21] We find no pixels showing a bad fit due to a foreground star. The Ω_* maps do not show conspicuous peaks, indicating that the foreground stars are not dominant, and the models successfully fit the galaxy emission.
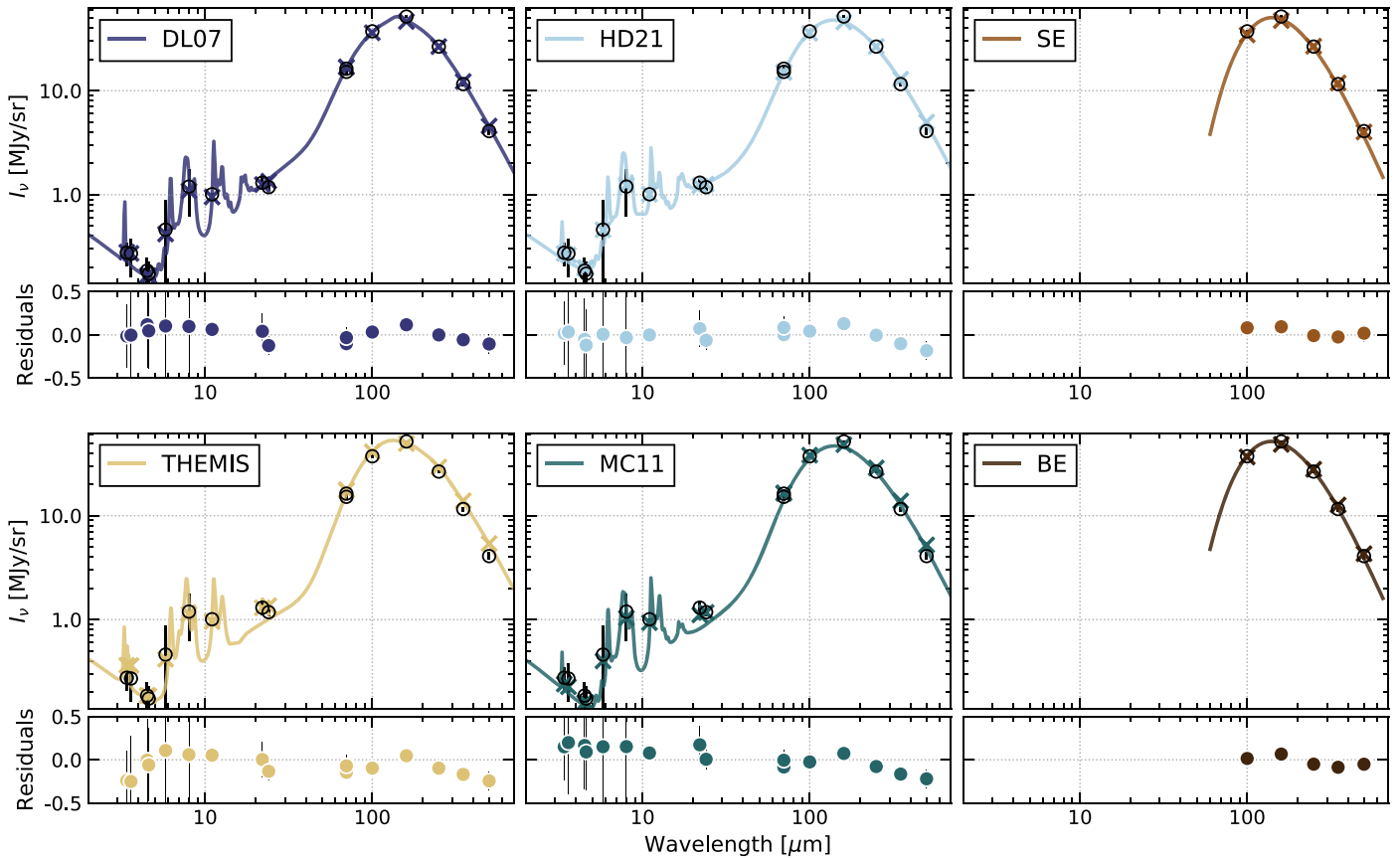
Figure 4. Example of the best fits in a pixel for the six models used in this study (color lines). The data are shown as empty symbols, with 1σ error bars. The synthetic photometry from the model spectrum is shown with a cross symbol, due to the band integration; this does not always sit exactly on the spectrum. The location of the measurement is marked by a cross in Figure 1.

In the process of masking, we first exclude the region within r_{25}, to mask the galactic emission. We then mask the brightest stars, using the star masks from Leroy et al. (2019) that leverage the known positions of stars from the GAIA and 2MASS catalogs.[22] To match the final products, we convolve and regrid these star masks to the SPIRE 500 resolution. After convolution, the mask values are no longer binary 0 and 1, but show intermediate values around the position of bright stars. We mask pixels above 0.15 to exclude these regions where bright foreground stars contaminate our measurements from the covariance matrix calculation.

One argument against the decision to mask bright stars to measure the covariance matrix would be that the emission from these stars is an astrophysical signal that should be taken into account to propagate the noise from a band to another. This would require creating a new noise model and significant changes to the fitting methodology. Rather than major changes to the fitting approach, we decide to mask the stars to measure the background covariance matrix.

5. Results

We investigate the differences in some of the key parameters from dust emission modeling when the models presented here are all used in an identical fitting framework. All residuals in this analysis are presented as (Data-Model)/Model. For radial profiles, we use the pixel size as the annulus width and cover

---

from the center of M101 to r_{25}. Appendix B shows the resolved maps of the fitted parameters for each model. Appendix C shows the residual maps of each model.

5.1. Quality of Fits

Figure 4 shows an example of the fits for each model in a single pixel (marked by the cross in Figure 1). In each panel, we plot the best-fit spectrum (colored lines) to the data SED (empty circles). The residuals are shown by the colored symbols. Negative residuals mean that the model overestimates the data. For example, the negative (and decreasing) residuals from 250 to $500\,\mu m$ in the physical model panels are representative of a systematic overestimation of the data (present also in other locations; see Appendix C, Figures 19–22). In Figure 5, we show the fractional residuals (Data-Model)/Model in each band for the pixels above the 3σ threshold. Appendix D shows the reduced χ^2 for all models.

The bulk of the residuals in the short-wavelength bands are within the instrument uncertainties and calibration errors. For example, despite the larger uncertainty due to the extended-source correction, the IRAC 8 band shows residuals mostly within 10%. Below $4\,\mu m$, THEMIS shows a clear offset that may be related to the absence, or low amount, of an ionized component in the HAC population, which leads to enhancement of the mid-IR features. It is also worth noting that these bands are dominated by starlight, modeled by a 5000 K blackbody, which is independent of the dust model itself. The residuals at $12\,\mu m$ are systematically positively offset by less

---
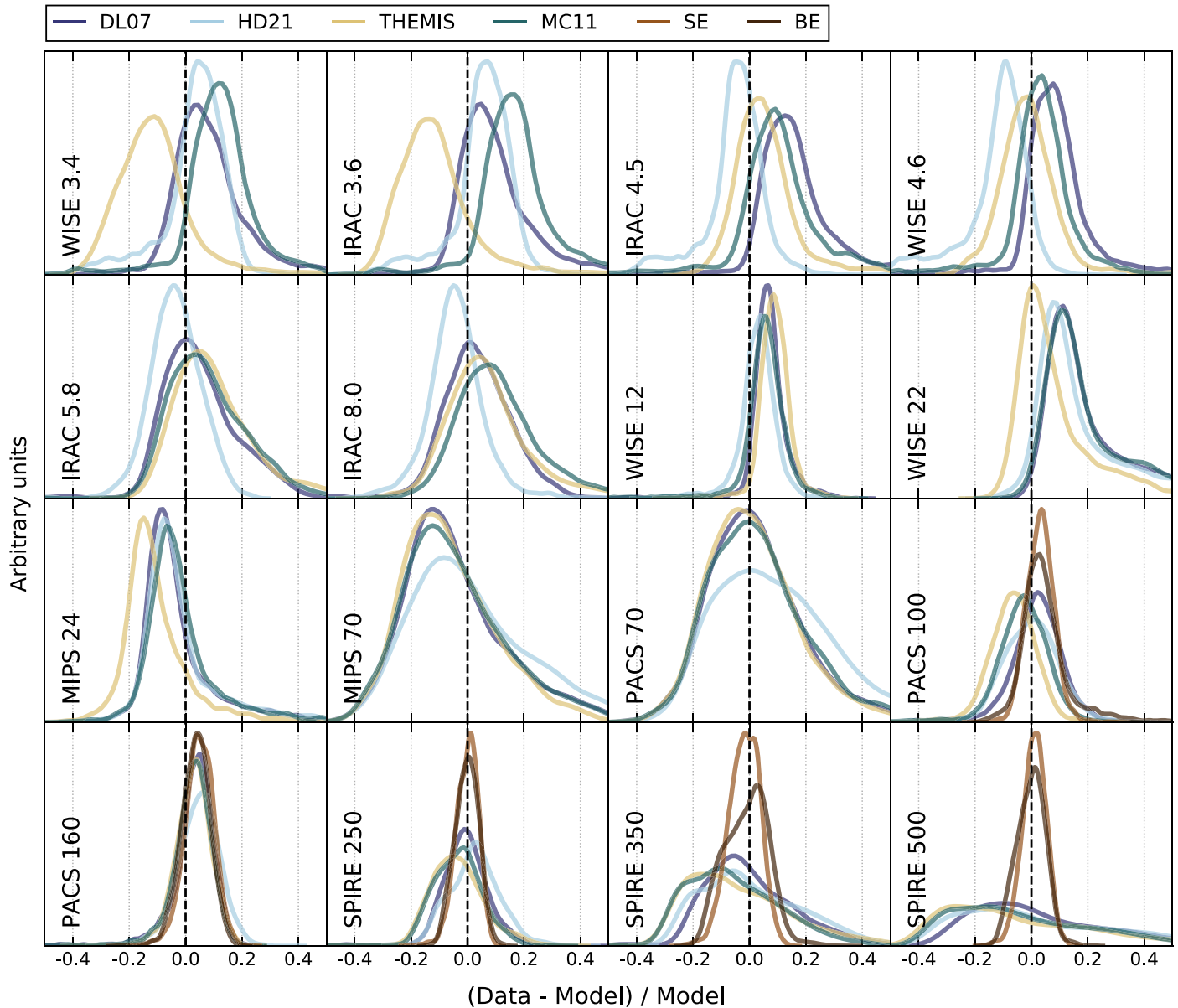
Figure 5. Fractional residuals (Data-Model)/Model for each model in each band. We plot the (Gaussian) kernel density estimates of the residual distributions. The WISE 12 band shows narrow, offset fits for all models while other mid-IR bands show clear over-/underestimations by some models. The physical models perform a good fit at 250 μm that gets progressively worse toward longer wavelengths. Only the modified blackbody models show systematically good fits, within 10%, in all far-IR bands, likely because of the spectral index, β being a free parameter.

than 10%, but all physical models show very narrow residual distributions. This is in contrast with the broader residuals in the IRAC 8 and WISE 22 bands, where we can see more differences between models.

All models show differences in the central values of the residual distribution at 100 μm. At 160 μm, all residuals overlap, and models perform fits of similar quality. At longer wavelengths, significant differences begin to appear. At all far-IR wavelengths, the modified blackbody models reproduce the SEDs the best. This is likely because of the additional parameter that can adjust the far-IR slope (β in the simple-emissivity model and β_2 in the broken-emissivity model). The SPIRE 250 band shows symmetrical residuals centered on 0 for the physical models (except THEMIS), while the residuals get progressively worse at 350 and 500 μm for all physical models,

showing that on average, the modeled far-IR slope of the SEDs is steeper than the data.

In the SPIRE 350 and SPIRE 500 bands, the large number of pixels underestimated by the models show residuals much larger than the uncertainties, ruling out statistical noise and indicating that the models are not able to fit these wavelengths. In the SPIRE 500 band, some of the pixels show the so-called "submillimeter excess" seen in other studies (e.g., Galametz et al. 2014; Gordon et al. 2014; Paradis et al. 2019).

5.2. Total Dust Mass and Average Radiation Field

We compute several galaxy-averaged quantities: the total dust mass $M_{\rm dust}$, the dust mass-weighted average radiation field $\langle \overline{U} \rangle$ for the physical models, and the mass-weighted average
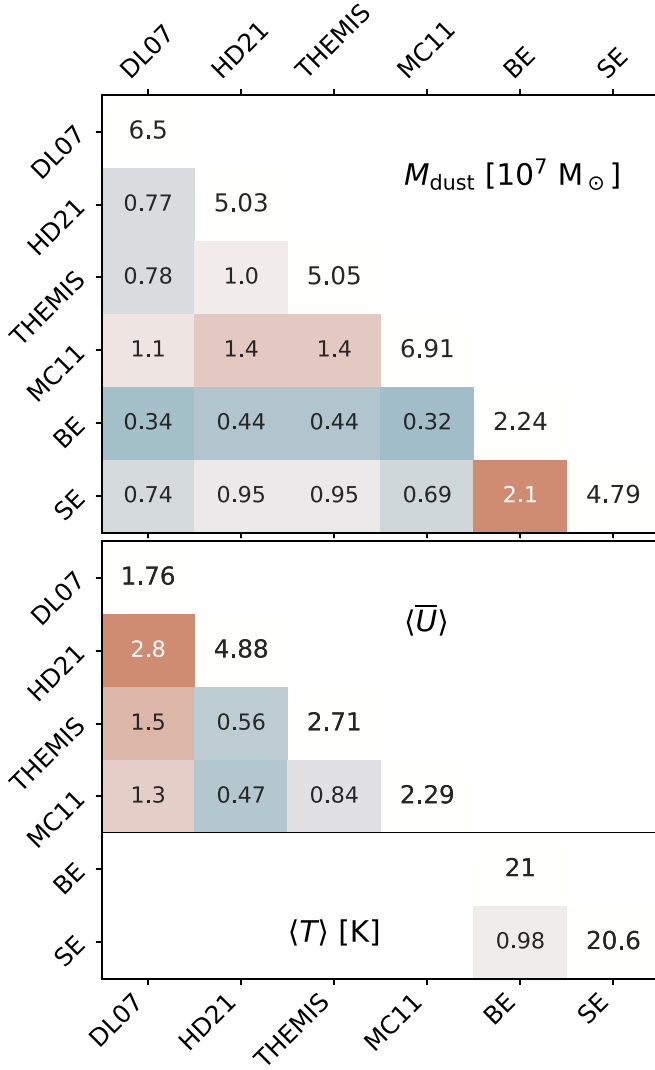
Figure 6. Integrated values (over the 3σ pixels). The diagonal elements show the total dust mass (top panel) and radiation field (bottom panel, above the line) or temperature (bottom panel, below the line). The off-diagonal elements are the ratios of the integrated values between different models and are read as "model Y-axis/model X-axis" (e.g., $M_{\rm dust}^{\rm HD21}/M_{\rm dust}^{\rm DL07} = 0.77$).

dust temperature $\langle T_{\rm dust} \rangle$ for the blackbody models. The average radiation field $\overline{U}$ is calculated for each pixel as

$$\overline{U} = (1 - \gamma)\, U_{\rm min} + \gamma \times U_{\rm min} \frac{\ln(U_{\rm max}/U_{\rm min})}{1 - U_{\rm min}/U_{\rm max}}, \qquad (13)$$

because we fixed $\alpha = 2$ (Aniano et al. 2020). The galaxy-integrated mass-weighted averages are calculated as

$$\langle \overline{U} \rangle = \frac{\sum_j \overline{U}_j \times \Sigma_{{\rm dust},\, j}}{\sum_j \Sigma_{{\rm dust},\, j}}$$

$$\langle T_{\rm dust} \rangle = \frac{\sum_j T_{{\rm dust},\, j} \times \Sigma_{{\rm dust},\, j}}{\sum_j \Sigma_{{\rm dust},\, j}}. \qquad (14)$$

The integrated values are calculated over the pixels above the 3σ detection threshold. In Figure 6, we show these measurements for each model as diagonal elements. We also provide the ratios between all models in $M_{\rm dust}$ and $\langle \overline{U} \rangle$ (or $\langle T_{\rm dust} \rangle$) to

explicitly show their differences. These off-diagonal elements read as Y-model/X-model (e.g., $M_{\rm dust}^{\rm HD21}/M_{\rm dust}^{\rm DL07} = 0.77$).

The top panel of Figure 6 shows the total dust masses. The broken-emissivity modified blackbody model yields the lowest total dust mass, while the MC11 model yields the highest. The simple-emissivity model shows a very different spatial variation of dust surface density from the other models (see Section 5.3). In a recent study of the KINGFISH sample, Aniano et al. (2020) found a total dust mass of $9.14 \times 10^7\, M_\odot$ (before their renormalization) by fitting the DL07 at MIPS 160 resolution ($\sim$39″).[23] Using the CIGALE SED fitting tool (e.g., Boquien et al. 2019 and references therein) and THEMIS, Nersesian et al. (2019) found a total dust mass of $4.70 \times 10^7\, M_\odot$, which is similar to the $5.05 \times 10^7\, M_\odot$ from THEMIS, in this study. It is worth noting that Nersesian et al. (2019) performed fits to the integrated SED, which could lead to a lower dust mass (Aniano et al. 2012; Utomo et al. 2019). However, low signal-to-noise pixels are included in the integrated SED and excluded in the resolved fits.

It is interesting to note that despite the fairly good agreement ($\sim$10%, Figure 5) of all physical models with each other (and modified blackbody models at far-IR wavelengths) in reproducing the data, the differences in dust masses can be much larger. This suggests intrinsic opacity values rather than fit quality dominate the differences between models in dust mass. This is supported by the recent extensive study done by Fanciullo et al. (2020). By comparing the literature opacities (including three models used in this work) with laboratory dust analog opacities, they found that dust masses can be overestimated by more than an order of magnitude.

The bottom panel of Figure 6 shows the integrated values for $\langle \overline{U} \rangle$ and $\langle T_{\rm dust} \rangle$. As expected, the HD21 model requires the highest radiation field, based on its colder dust. THEMIS and the MC11 model show similar values of $\langle \overline{U} \rangle$. Nersesian et al. (2019) found a dust temperature of 21.7 K by fitting a modified blackbody (with the THEMIS opacity), close to that yielded by the modified blackbody models here.

The mass-weighted average temperatures correspond to radiation fields of 2.5 and 2.3 (using Equation (8)) for the broken-emissivity and the simple-emissivity models, respectively. They are in good agreement with the radiation field values fitted by the physical models.

5.3. Dust Surface Density, Σ_{dust}

Figure 7 shows maps of the dust surface density, $\Sigma_{\rm dust}$, for each model, as well as their ratios with each other. We can see that the physical dust models DL07, HD21, THEMIS, and MC11 are all fairly close to each other (light colors), with variations in dust surface density within a factor of 2. They all yield similar dust surface density structures and appear to vary from one another by a spatially smooth offset. THEMIS and the HD21 model show the closest $\Sigma_{\rm dust}$ values but show an inversion of their ratio around $0.38\, r/r_{25}$, where THEMIS requires less dust (see Figure 12). The HD21/DL07 and MC11/THEMIS ratio maps are particularly flat, with ratios of $\sim$1.3–1.4 in both cases, pointing at the resemblance in their large grains properties and size distribution. The MC11 model requires the most dust mass. This is consistent with the comparison analysis in Chastenet et al. (2017). The dust surface

---
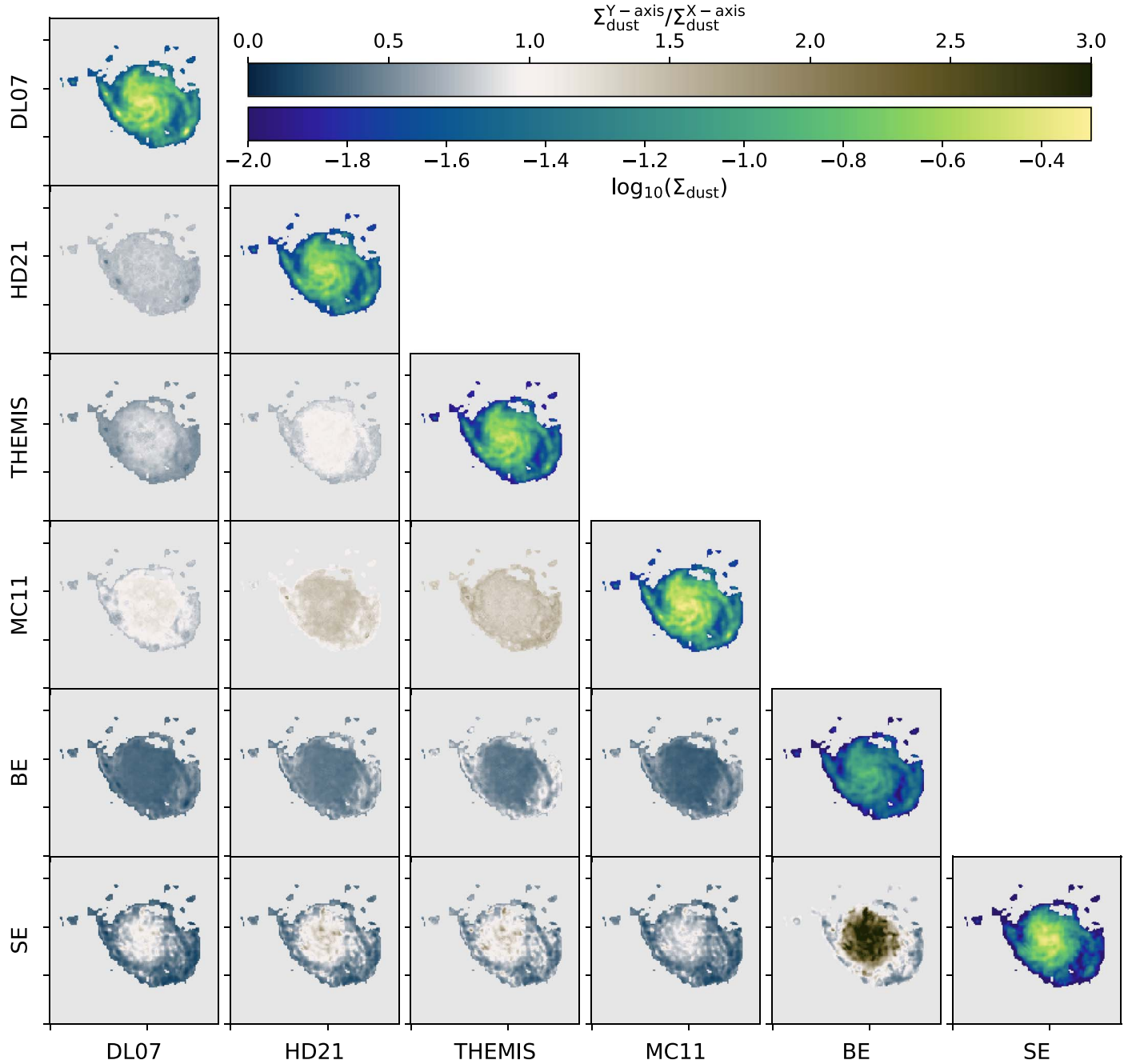
Figure 7. Dust surface density maps (diagonal) and corresponding ratios with each model. The MC11 model requires the largest dust mass, followed by the simple-emissivity and DL07 models. All physical dust models show very similar spatial variations despite having different values of Σ_{dust}. The HD21/DL07 and MC11/THEMIS ratio maps are particularly smooth across the disk, but the MC11/DL07 and THEMIS/HD21 have the ratios closest to 1. The simple-emissivity model shows clear structural differences with the other models by requiring a lot of dust in the center, but rapidly dropping in the outskirts.

density from the broken-emissivity model is consistently lower than the physical dust models. It shows a rather smooth offset, which indicates that the spatial variations are fairly similar between them. The dust surface density from the simple-emissivity model shows different spatial structures in the center and the outskirts of the galaxy. It yields high Σ_{dust} values in the center but drops more rapidly than any other model with increasing radius (Figure 12; see also Chiang et al. 2018).

A caveat of our approach is the difference in treating the heating of dust grains between physical dust models and modified blackbodies. In the latter, we only use a single temperature, which is not equivalent to the ensemble of radiation fields used in the physical models. However, given

the two extreme behaviors of the modified blackbodies (the simple-emissivity model requiring a high dust mass, and the broken-emissivity model requiring the lowest), it is not obvious that the use of multiple temperatures (or radiation fields) drives the differences in dust mass observed here. Rather, the calibration of the modified blackbodies, and their effective opacity, seems to be more important.

5.4. Average Radiation Field, $\overline{U}$

We perform the same ratio analysis with $\overline{U}$, derived from the fitted parameters in the physical dust models (Equations 13 and 14). In Figure 8, we show the radial profiles for $\overline{U}$, as well as the
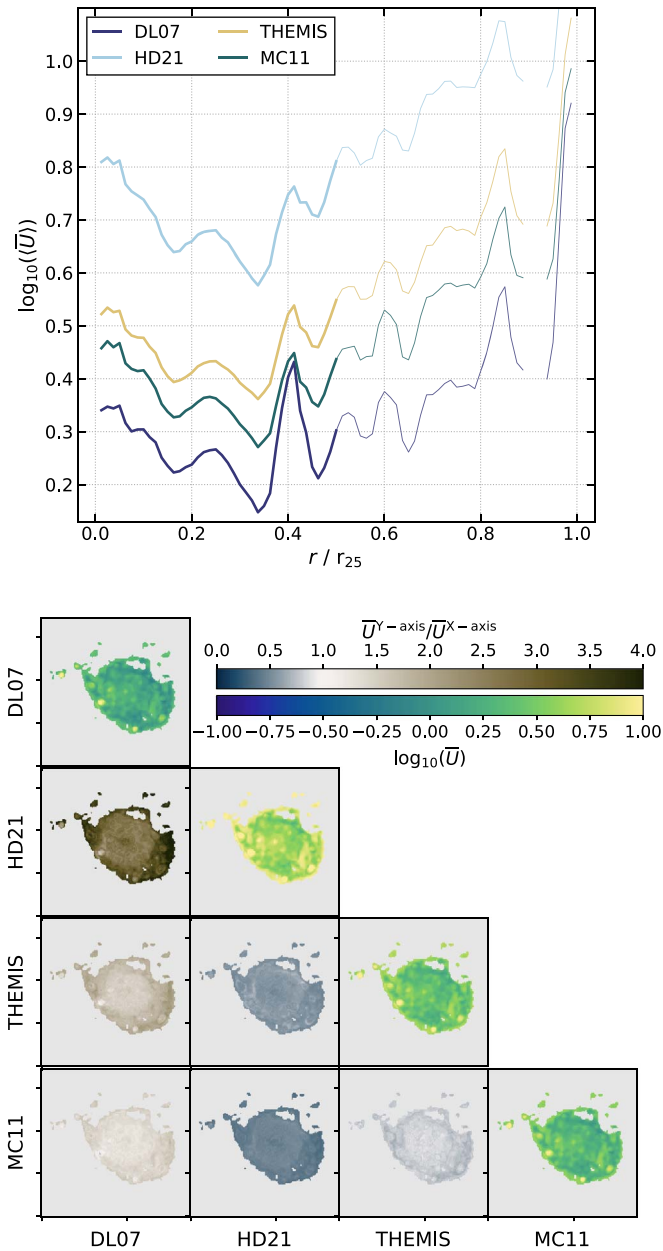
Figure 8. Top: radial profile of $\langle \overline{U} \rangle$ (mass-averaged radiation field; see Equation (14)) for each physical model. The thick lines stop where the radial profile is affected by the selection effect due to fitting only bright pixels (Section 4.2.2). Bottom: average radiation field, $\overline{U}$, maps (diagonal), and corresponding ratios with each model. The HD21 model shows the highest values of $\overline{U}$ in all pixels. Despite different values, all models show a very similar spatial distribution of $\overline{U}$, including in H II regions.

parameter maps and the ratios of each model. In the radial profile, the thick lines stop where the selection effect due to fitting only bright pixels becomes important. Using the SPIRE 500 image, we found that the radial profile of IR emission for all pixels and for fitted pixels only differ significantly at $\sim 6'$ (i.e., $0.5\,r_{25}$). The variations in $\overline{U}$ are reflective of those of U_{min}, because the γ values are overall small, lending more power to the delta function than the power law (Equation (7)).

The overall variations of $\overline{U}$ appear to be rather smooth, which is expected because it is dominated by the diffuse radiation field U_{min}. However, we do find enhanced values of $\overline{U}$ in H II regions. The ratio maps do not strongly show these peaks, which indicates that all models behave similarly and

require higher radiation field intensities in these regions. As for the Σ_{dust} parameter, the ratio maps for $\overline{U}$ do not display any conspicuous spatial differences, but rather an offset between each model. This is also visible in the upper panel of Figure 8.

The HD21 model shows the highest values of $\overline{U}$. This is expected as the dust in the model is "colder" than other models, due to very few large carbonaceous grains. This leads to a higher radiation field intensity required to reach the same luminosity.

The spatial distributions of the γ parameter are similar in all physical models, and we chose not to show them. Instead, we use the average radiation field, $\overline{U}$, which includes γ in its calculation. The HD21 model shows the lowest values of γ, which, combined with the highest values of U_{min}, means it requires more power in the delta function than the other physical models.

5.5. Fraction of PAHs

Three models have an explicitly defined PAH fraction. The DL07 and HD21 models define the parameter q_{PAH} as the fraction of dust mass contained in carbonaceous grains with less than 10^3 carbon atoms, roughly less than 1 nm in size. We use the f_{PAH} parameter from the MC11 model to estimate a PAH fraction, i.e., the mass of grains with sizes from 0.35 to 1.2 nm, as defined by the fiducial parameters. We refer to the mid-IR emission feature carriers in THEMIS as HACs. We use the definition in Lianou et al. (2019) to compute a fraction of HACs from THEMIS results, which can compare to the PAHs in other dust models: they found that this fraction of HACs corresponds to grains between 0.7 and 1.5 nm of the sCM20 component. It is important to remember that the strict definition of the PAH/HAC fraction is different in each model, but its purpose—fitting the mid-IR emission features—remains similar.

We investigate the variations of the surface density of the carriers, Σ_{PAH} and Σ_{HAC}, instead of their abundances. In the top panel of Figure 9, we show the radial profiles of $\Sigma_{\{PAH;\,HAC\}}$. Although the absolute values of the surface density of PAHs (HACs) differ by a factor of up to ~ 3.5 (similar to dust masses), their gradients are very similar. This behavior shows that the grain populations that are held responsible for the mid-IR features in each model follow comparable distributions. In these models, their contributions to the total dust mass vary significantly but all prove to be a good fit to the mid-IR bands (see also Figure 5). This is also exemplified by the normalized ratio maps in Figure 9 (bottom panel). The dark colors in the outermost pixels of the HD21 model are due to the best q_{PAH} fit consistent with 0%. To visualize the variations between models, we normalize each parameter map to their mean value (as shown in the color-bar labels). We are thus able to compare the spatial variations of the maps and avoid the offsets due to the definition differences of PAHs or HACs.

The q_{PAH} map in Aniano et al. (2020, using the DL07 model) shows similar features to ours. A large portion of the disk of M101 has a rather constant distribution of q_{PAH}, with conspicuous drops in H II regions. In their study using the Desert et al. (1990) dust model, Relaño et al. (2020) found a flat radial profile of the small-to-large grain mass ratio, up to $0.8\,r_{25}$ ($\sim 9'.1$). Our maps of the fraction of PAHs, or HACs, present a somewhat flat distribution (variations less than 1%) out to $\sim 0.3\,r_{25}$ ($\sim 3'.4$; see Appendix B) and a steep change farther out.

5.6. Reproducing the Mid-IR Emission Features

To investigate in more detail the ability of each physical model to reproduce the PAH features, we perform a fit on an integrated
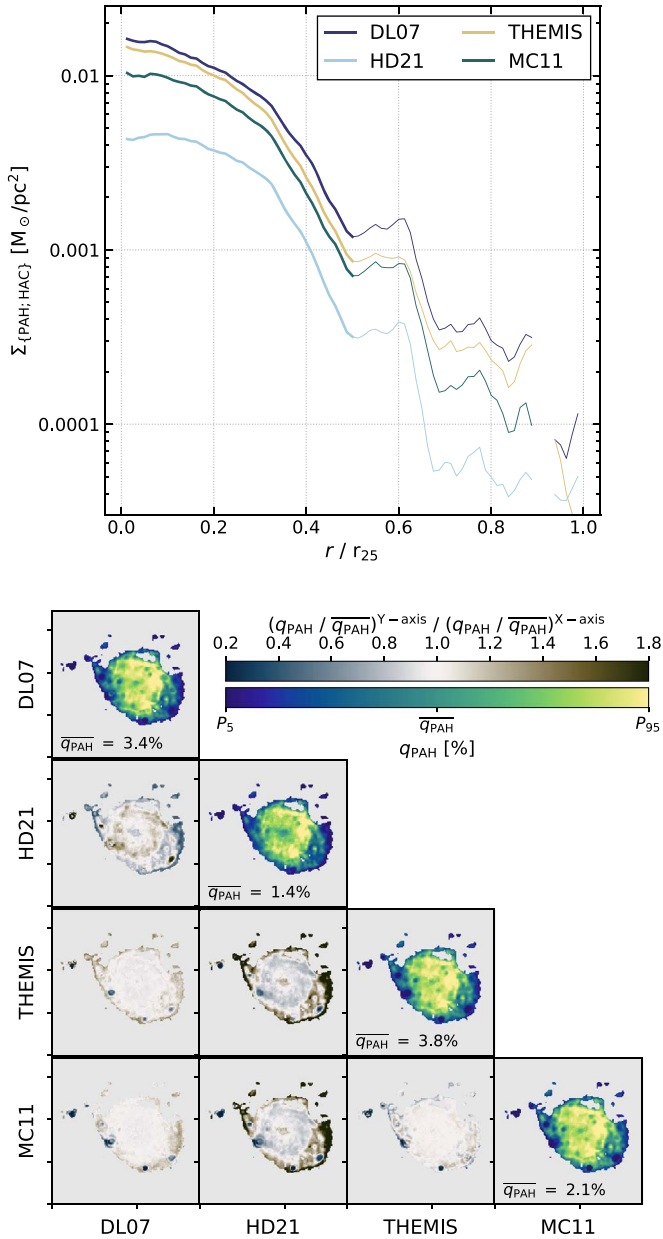
Figure 9. Top: radial profiles for Σ_{PAH}, or Σ_{HAC}, in $M_{\odot}\,pc^{-2}$. The models yield very similar spatial variations. This indicates that the definition of the feature carriers matters in terms of their contribution to the total dust mass, but they all reproduce the mid-IR features similarly. The thick lines stop where the radial profile is affected by the selection effect due to fitting only bright pixels (Section 4.2.2). Bottom: fraction of PAHs (or HACs; diagonal) centered on their respective mean value, with boundaries at the 5th and 95th percentiles (P_5, P_{95}). The normalized ratios (normalized to the mean; off-diagonal) show the spatial variations between models.

SED and compare the results to measurements from the Infrared Spectrograph (IRS; on board Spitzer) in that same region (J. D. T. Smith 2021, private communication). Figure 10 shows a zoom on the mid-IR part of the models and the results of the fits to the integrated SED. From that fit, it appears that all models are able to generally reproduce the mid-IR features, with their different parameters, but we can notice a few differences between models.

From the residuals (bottom panel), we see that the models perform similarly at 5.8, 8.0, and 12 μm. At 22 and 24 μm, the offset between the measurements means the models tend to split the difference and sit between the points. We note that all models appear to overestimate the continuum around 7 μm, in between the 6.2 and 7.7 μm PAH features.

There are nonetheless a couple of noticeable differences between each model. For instance, the HD21 model shows a higher continuum at 10 μm than the other three models, despite a similar continuum at 20 μm. This rules out the higher U_{min} found in the HD21 model as the reason for the higher flux at 10 μm. Rather, in this model, the emission at 10 μm is strongly dependent on the amount of nanosilicates used to account for the lack of correlation between PAH emission and anomalous microwave emission (Hensley & Draine 2017). The ratio between the flux at 20 and 10 μm is $\sim$1.7 for the HD21 models and 2 or above for the other three models. On the other hand, THEMIS shows no emission feature around 17 μm, while the other models do (although it has no impact on this particular fit). Around 7 μm, all models show a higher flux than the one seen in the IRS spectrum.

It is notable that, using only photometric bands from WISE and Spitzer /IRAC in the fit, all models reasonably reproduce well the mid-IR emission features, despite having different values of the PAH (or HAC) fraction and different definitions of the carriers. However, the comparison to spectroscopic measurements shows that there are still differences between models.

### 5.7. SPIRE 500 and Σ_{dust}

The monochromatic dust emission in far-IR wavelengths has often been used as a mass tracer of the ISM (e.g., Eales et al. 2012; Groves et al. 2015; Berta et al. 2016; Scoville et al. 2017; Aniano et al. 2020; Baes et al. 2020). In Figure 11, we plot the emission of M101 at 500 μm as a function of the fitted Σ_{dust} for each model (pixels above the 3σ detection threshold), color-coded by the minimum radiation field U_{min} or dust temperature T_{dust}.

In all cases, we can see two distinct relations as the SPIRE 500 emission increases. The majority of the fitted pixels show a linear scaling between the emission at 500 μm and Σ_{dust}, while in some specific regions of the galaxy, all models prefer a higher radiation field (or temperature) and a lower dust surface density. We provide the scaling relations between the emission at 500 μm in MJy sr^{-1}, and the dust surface density in $M_{\odot}\,pc^{-2}$, for each model. We measure the 5th and 95th percentiles of the data points above the 3σ detection threshold (to keep the bulk of the distribution only). We fit a linear slope to these points:[24]

$$
\begin{aligned}
\log_{10}(\Sigma_d)^{DL07} &= 1.21 \pm 0.01 \times \log_{10}(I_\nu^{500\,\mu m}) \\
&\quad -1.38 \pm 0.005 \\
\log_{10}(\Sigma_d)^{MC11} &= 1.25 \pm 0.02 \times \log_{10}(I_\nu^{500\,\mu m}) \\
&\quad -1.39 \pm 0.008 \\
\log_{10}(\Sigma_d)^{THEMIS} &= 1.32 \pm 0.02 \times \log_{10}(I_\nu^{500\,\mu m}) \\
&\quad -1.56 \pm 0.008 \\
\log_{10}(\Sigma_d)^{HD21} &= 1.21 \pm 0.01 \times \log_{10}(I_\nu^{500\,\mu m}) \\
&\quad -1.50 \pm 0.006 \\
\log_{10}(\Sigma_d)^{SE} &= 1.61 \pm 0.03 \times \log_{10}(I_\nu^{500\,\mu m}) \\
&\quad -1.80 \pm 0.02 \\
\log_{10}(\Sigma_d)^{BE} &= 1.08 \pm 0.08 \times \log_{10}(I_\nu^{500\,\mu m}) \\
&\quad -1.78 \pm 0.005.
\end{aligned}
$$

$$(15)$$

To identify the pixels that "branch out" from the bulk, we select any pixel that falls below one standard deviation from the

---

[24] The fit coefficients and uncertainties were measured using the `numpy.polyfit` procedure.
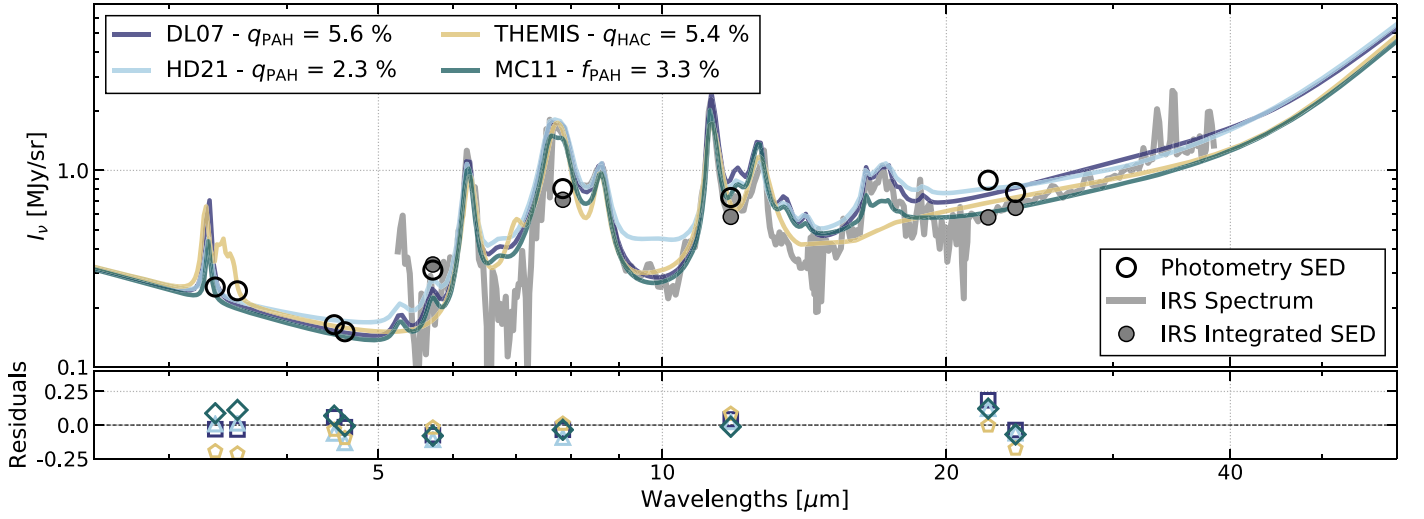
Figure 10. Fits to the integrated SED from the broadband photometry (open circles) within a rectangle box (drawn in Figure 1). The Spitzer/IRS spectrum and its corresponding SED (convolved in the 16 bands used here) are shown in gray (line and filled circles). All models perform a good fit to the mid-IR part of the SED but show different fractions of PAHs (or HACs). Differences can be noticed between models: a higher 10 μm emission in the HD21 model, due to nanosilicates, or the lack of an emission feature at 17 μm in THEMIS.
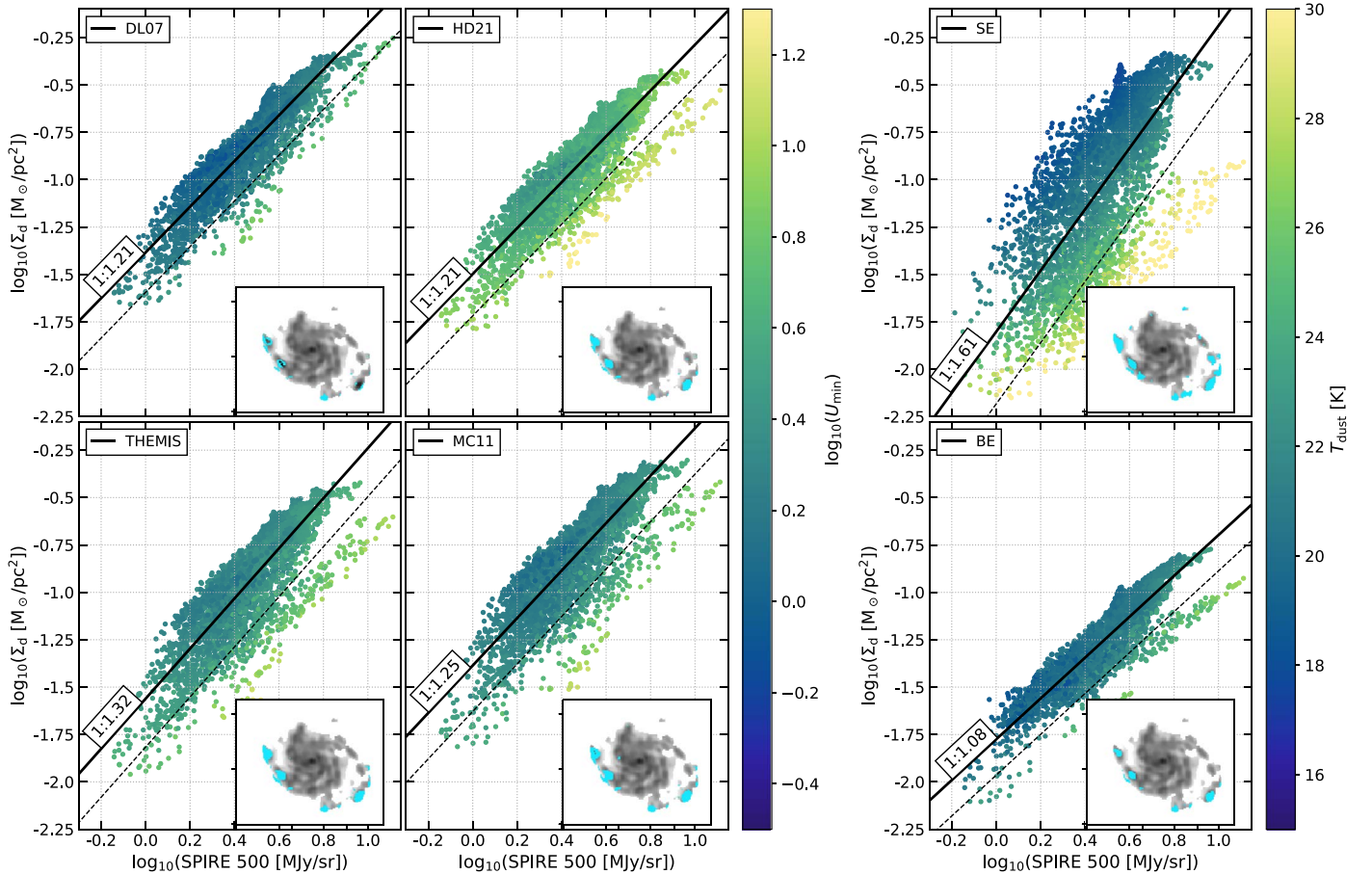
Figure 11. SPIRE 500 emission as a function of the fitted $\Sigma_{\rm dust}$ for each model, color-coded by the radiation field $U_{\rm min}$ or the dust temperature $T_{\rm dust}$. We identify a separation in the linear scaling of $\Sigma_{\rm dust}$ with the dust emission at 500 μm, marked by the dashed lines. The pixels below the lines are plotted in color in the maps and are located in H II regions and surroundings. In these specific locations, the luminosity does not follow the same relation with $\Sigma_{\rm dust}$ as the rest of the galaxy.

fit (dashed lines). In each panel, we show the spatial location of these pixels. It becomes clear that the regions that need a higher $U_{\rm min}$ (or $T_{\rm dust}$) are H II regions and in the outskirts of the galaxy. These pixels can account for between 4% and 11% of the pixels above the 3σ detection. The branching-out from the main

relation is likely the consequence of the fact that the dust in these H II regions is significantly hotter than average (as shown by the enhanced $\overline{U}$ in all models in Figure 8). Lower dust-to-gas ratios in the galaxy outskirts may also contribute to this trend.

In Aniano et al. (2020), the authors found that this relation is well represented by a power-law scaling in the KINGFISH sample, with a slope of 0.942, which is lower than our measured value of 1.2 for M101 with the DL07 model. A linear slope would be expected if the dust temperature and optical properties were uniform throughout the galaxy, leading to a constant $I_\nu^{500}/\Sigma_{dust}$ ratio. The spatial distribution of temperatures throughout each individual galaxy leads to distinct slopes, and for M101, we find that in regions of higher dust surface density, the dust is also warmer, leading to more 500 μm emission (this can be seen in the change in the color table in Figure 11 at the highest Σ_{dust}). The branch of H II region points we see represents only a small fraction of the total data and may not be evident on the Aniano et al. (2020) plot.

6. Model Performance Given Abundance Constraints on Dust Mass

6.1. Maximum Dust Surface Density

The calibration of dust models involves a constraint on elements locked in grains (see Section 2.3). This step relies on depletion measurements, which characterize the distribution of heavy elements between the gas and solid phases. The final amount of elements allowed in dust grains varies between different physical dust models. The final dust masses derived by each model vary as well, as discussed in Sections 5.2 and 5.3.

A way to assess the performance of dust models is to verify that the required dust mass does not exceed the available heavy element mass, as constrained by metallicity measurements (e.g., Gordon et al. 2014; Chiang et al. 2018). We perform this test in M101 because its metallicity gradient has been thoroughly characterized (e.g., Zaritsky et al. 1994; Moustakas et al. 2010; Croxall et al. 2016; Berg et al. 2020; Skillman et al. 2020).

We estimate the dust mass surface density upper limit by assuming all available metals are in dust and calculating the metal mass surface density from the metallicity gradient and observed gas mass surface density:

$$\frac{M_{dust}^{max}}{M_{gas}} = \frac{M_Z}{M_{gas}}, \qquad (16)$$

where M_{gas} and M_Z are determined as follows.

The gas surface density is the sum of H I and H$_2$ surface densities including a correction for the mass of He (we ignore the ionized gas contribution). The latter is built from CO emission, assuming two prescriptions for the CO-to-H$_2$ conversion (see Section 2). We include the MW α_{CO} prescription as it is widely used (Equation (1)). We also choose the α_{CO} prescription from Bolatto et al. (2013), which takes into account environmental variations of α_{CO} with metallicity and surface density (Equation (2)). We emphasize that the Σ_{dust} upper limit in this section is dependent on the choice of α_{CO} to derive a gas surface density. This is particularly true in the central region of M101, where H$_2$ dominates (e.g., Schruba et al. 2011; Vílchez et al. 2019) and where the two α_{CO} differ the most. Note also that this result differs from that of Chiang et al. (2018). This is expected as the α_{CO} conversion factor in their study (from Sandstrom et al. 2013) is lower than the ones used in this study, which leads to a lower upper limit.

We use the $12 + \log_{10}(O/H)$ radial profile from Berg et al. (2020) and convert it to metallicity through

$$\frac{M_Z}{M_{gas}} = \frac{\frac{m_O}{m_H} 10^{(12+\log_{10}(O/H))-12}}{1.36 \frac{M_O}{M_Z}}, \qquad (17)$$

with m_O and m_H the atomic masses of oxygen and hydrogen, respectively, and the oxygen-to-metals mass ratio $M_O/M_Z = 0.445$ (Asplund et al. 2009).

The top panels in Figure 12 show the radial profile of Σ_{dust} for each model and the Σ_{dust}^{max} upper limits yielded by the two α_{CO} prescriptions used here (black lines, dotted and dashed–dotted). We see on the top-left panel that the DL07 and MC11 models are above both Σ_{dust}^{max} upper limits in almost all of the significant pixels. THEMIS and the HD21 models are fairly in line with the Bolatto et al. (2013) upper limit, with the conservative assumption that 100% metals are in dust grains. These behaviors suggest that the dust emissivity in all physical models is too low, which leads to requiring too much dust. We note that the large dust masses are likely due to the opacity calibration rather than a wrong fit in the far-IR bands: in Figure 5, all physical models show a reasonable fit at 160 μm, much closer to the IR peak than the 500 μm band. We are confident that the IR peak is correctly recovered and that the high dust masses are not due to the submillimeter excess. Based on the reasonable quality of the fits, we believe that the excessive mass is likely due to the opacity calibration.

6.2. (Re)Normalization

Despite sharing a common calibration approach, the details of the opacity calibration in the dust models used in this study vary in small but significant ways. While all models were calibrated to MW diffuse emission, they did not use exactly the same high-latitude cirrus spectrum. In addition, the M_{dust}/M_H adopted for the MW diffuse ISM by the physical dust models varies. Additionally, the radiation field that best reproduces the MW diffuse emission, U^{MW}, differs slightly from one model to the next. Because of the relationship between dust temperature and radiation field ($U \propto T_{dust}^{4+\beta}$) and dust temperature and luminosity, even a slight difference in the assumed radiation field may lead to a significant change in the model's calibrated dust opacity.

To investigate calibration discrepancies, we renormalize each of the dust models via a fit to a common MW diffuse emission spectrum using the same abundance constraints. We use the MW SED described in Gordon et al. (2014), which we previously used to calibrate the κ_ν of the modified blackbody models (Chiang et al. 2018). This SED is the same as that used in Compiègne et al. (2011), a combination of DIRBE and FIRAS measurements (e.g., Boulanger et al. 1996; Arendt et al. 1998).[25] We do not use the ionized gas correction because depletion measurements do not correct for it, and instead use a correction factor of 0.97 for molecular gas only (Compiègne et al. 2011). We integrate the SED in the PACS 100, PACS 160, SPIRE 250, SPIRE 350, and SPIRE 500 bands, so all models use the same wavelength coverage. We use 2.5%

---

[25] Although more recent measurements from Planck are available in the far-IR, we emphasize here that the important aspect is about uniformity. We choose the DIRBE+FIRAS SED as it is conveniently the one used to calibrate the modified blackbody models. Additionally, the significant input brought by Planck measurements are past the wavelength range used in our study (submillimeter and millimeter range).
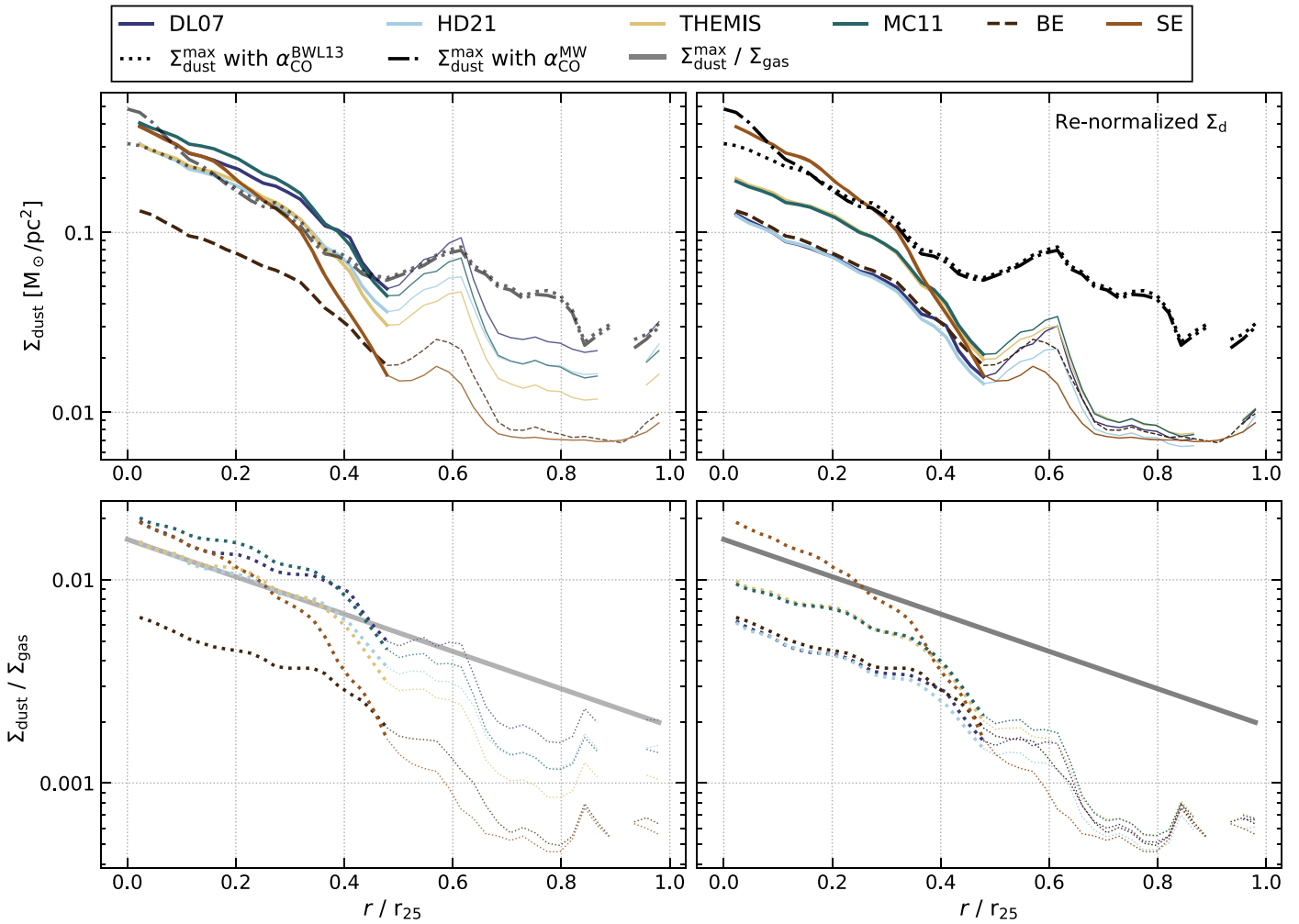
Figure 12. Top: radial profiles for Σ_{dust} (colored lines) and dust surface density upper limits (black dotted and dashed–dotted lines). Upper limits are estimated from gas and metallicity measurements, assuming all metals are locked in dust grains (Section 6.1). We have projected the dust surface density maps to the gas maps' pixel grid and masked the gas maps where there are no dust data (to ensure we are selecting identical pixels in building radial profiles). The upper limits are invariant between the left and right panels. Left: radial profiles from the fits. All physical models and the simple-emissivity model are either above or similar to the upper limits, out to 0.4 r/r_{25}. Right: renormalized dust surface densities for the physical models (Section 6.2). The renormalization forces physical models to the same abundance constraints ($M_{dust}/M_H = 1/150$) and to fit the same diffuse MW IR emission. Doing so, we derive correction factors and apply them to the dust surface densities, scaling them down to plausible values (below the Σ_{dust}^{max} lines). Bottom: dust-to-gas ratios for each model, assuming the gas surface density derived with α_{CO} from Bolatto et al. (2013). The gray line represents the upper limit from Berg et al. (2020) and assuming a dust-to-metal ratio of 1 (Equation (17)). The thick lines stop where the radial profile is affected by the selection effect due to fitting only bright pixels (Section 4.2.2), creating the conspicuous features in the H II region locations. The main bump at 0.6 r/r_{25} corresponds to the two H II regions NGC 5447 and NGC 5450. The less visible bump at 0.5 r/r_{25} corresponds to the H II region NGC 5462.

uncorrelated and 5% correlated errors to account for FIRAS and DIRBE uncertainties (Gordon et al. 2014). The M_{dust}/M_H ratio set in the normalization is $1/150$, as suggested by depletion studies ($F_* = 0.36$ from Jenkins 2009, see also Gordon et al. 2014).

To perform the renormalization using the MW SED, we use the same fitting technique as previously described with the following choices: (1) we do not use the combination of radiation fields nor the stellar component (i.e., $\Omega_* = \gamma = 0$). (2) We allow the minimum radiation field U_{min} and the total dust surface density Σ_{dust} to vary in each physical model. (3) We keep the relative ratios between grain populations fixed and do not vary them independently (e.g., for each model, we use the total spectra solid lines "DL07," "HD21," "MC11," and "THEMIS" in Figure 2).

The fits yield renormalization factors that correct all physical models from their respective assumptions to a dust-to-H ratio of 1/150. These corrections range from 1.5 for THEMIS, to 3

for the DL07 model (see Appendix A). With this normalization, we are able to meet the metallicity constraints. The top-right panel of Figure 12 shows the radial profiles with the correction factors applied to the surface densities of the physical dust models. The renormalization brings the models to lower dust surface densities that agree with the upper limit based on the metal content. It is interesting to note that the renormalized models now show three distinct behaviors in the dust mass surface density radial profile: DL07, HD21, and the broken power-law emissivity modified blackbody yield very similar results; THEMIS and MC11 are very similar to each other and offset by a factor of $\sim$2 from the first group, and the simple power-law emissivity modified blackbody has a steeper increase that still puts it above the abundance constraints even though it is similarly normalized to the MW cirrus spectrum. The two different behaviors, for DL07 and HD21, and for THEMIS and MC11 are likely due to the difference in

the best $U_{\min}^{MW}$ to fit the MW SED, and their initial spectrum used for calibration.

In the bottom panels of Figure 12, we show the radial profile of the dust-to-gas ratios (DGR) for each model, using the α_{CO}^{BWL13} conversion factor. The bottom left shows the DGR with the derived dust surface densities, and the bottom-right panels are after renormalization. The thick gray line shows the upper limit of the DGR using the metallicity gradient from Berg et al. (2020) and Equation (17), with α_{CO}^{BWL13}. We find the same abrupt change in the DGR as Vílchez et al. (2019) around $0.5\, r_{25}$, although with slightly lower values, consistent with the higher dust surface densities in this study.

7. Discussion

Here we discuss some next steps that should be undertaken to improve dust emission modeling. In the previous sections, we investigated some systematic effects linked to the modeling choices.

We showed that physical dust models are likely to require too much dust mass, exceeding what is available based on metallicity measurements (for reasonable choices of CO-to-H$_2$ conversion factors, though we note that, in the central region, this assertion is strongly dependent on this choice). This excess is linked to the calibration of these models, in particular, the elemental abundances prescribed, and their assumed radiation field. Combined with the growing number of metallicity measurements in nearby galaxies (e.g., Kreckel et al. 2019; Berg et al. 2020), additional constraints for external environments (beyond the MW) may help to perform better fits of dust emission.

Several aspects of galaxy evolution studies rely on grain properties. Dust evolution models rely heavily on observational constraints to find the parameters that best match the observed properties of dust. The balance between destruction and formation processes in dust evolution models are adjusted by observed dust masses, which need to be accurately measured (e.g., by emission fitting). Similarly, dust-to-gas ratio evolution with metallicity is often derived using dust masses from emission measurements (e.g., Rémy-Ruyer et al. 2014; De Vis et al. 2019; Nersesian et al. 2019; De Looze et al. 2020; Nanni et al. 2020) and are subject to the systematic biases found in this work.

Our study was designed for a rigorous comparison between models fit to mid- through far-IR SEDs. Several choices made in this study are justified by our implementation of each model in the most similar framework possible. This also requires using a uniform radiation field description, and the parameters that go into describing the physical dust models in their fiducial form are not always adapted to the choice of the radiation field model of this work (Equation (7)).

Because of the limited wavelength coverage and SED sampling of this study, we "tie" together different grain populations, based on the similarity of their respective emission spectra. In MC11, the large carbon (LamC) and silicate (aSil) grains have very similar slopes in the far-IR, which would make these fit parameters strongly degenerate if both were allowed to vary. In THEMIS, the key difference between the large carbon grains (lCM20) and the large silicate grains (aSilM5) is their slopes in the far-IR: the lCM20 grains have a flatter SED than aSilM5. However, the spectral coverage used in this study is too limited to properly constrain the emission from the two grain populations. These choices have

implications for the evolution of dust composition in the ISM because the ratios of carbon-to-silicate in large grains are assumed to be constant for each model of this study.

Additionally, our further tests show that the γ parameter is degenerate with the emission of some of the grain population in MC11 and THEMIS. The abundance of small amorphous carbon (SamC) in MC11 helps adjust the slope between 24 and 70 μm. In the radiation field parameterization chosen for this study, the γ parameter has a similar impact on the shape of the dust emission. Keeping both the small amorphous carbon grains abundance and γ as free parameters introduces a degeneracy in the fitting. For this reason, we choose to keep the fiducial relative abundances of SamC with respect to that of big grains (LamC+aSil) fixed. In THEMIS, when allowing both lCM20 and aSilM5 populations to vary (e.g., with f_{aSil}, the fraction of large grains in the form of aSilM5), we also introduce a degeneracy with the γ parameter. A varying ratio of carbon-to-silicate grains induces a similar change in the SED shape and both parameters, and γ and f_{aSil} become slightly degenerate. Future studies with more wavelength coverage and more detailed constraints on individual elemental abundances may be able to allow for more free parameters in the fits.

8. Conclusions

In this study, we compared the dust properties of M101 derived from six dust models: four physical dust models and two blackbody models. We used the models from Draine & Li (2007), Compiègne et al. (2011), Jones et al. (2017, THEMIS), and HD21, as well as simple-emissivity and a broken-emissivity modified blackbody models to assess the differences in various dust properties yielded by fitting the mid- to far-IR emission from WISE, the Spitzer Space Telescope, and the Herschel Space Observatory photometry. Our main conclusions are:

1. There are a few notable trends in the fitting residuals (described as (Data-Model)/Model; Figure 5). All physical models reproduce the mid-IR bands within 10%, with very similar residual distributions in the WISE 12 band. All models perform fits of similar quality at 160 μm. While the modified blackbody models can reproduce the data in all far-IR bands (residuals centered on 0), the fits from physical models have large residuals at long wavelengths. This suggests that the flexibility to adjust the long-wavelength slope of the opacity is important to reproduce the observed SEDs.
2. All physical models reproduce the mid-IR emission features but yield different values of the mass fraction of their carriers (Figure 9). Models that attribute the mid-IR emission features to PAHs or HACs do similarly well in reproducing the mid-IR spectrum.
3. We provide the scaling relation of $\Sigma_{dust} = f(I_\nu^{500\,\mu m})$ and identified a diverging relation in H II regions, where hot dust changes the relationship between dust emission and mass (Figure 11).

Examining the fitting results of total dust masses and dust surface density distributions, we find:

1. Models yield different total dust masses, up to a factor of 1.4 between physical models, and up to 3 including modified blackbodies (Figure 6), but all show similar spatial distributions of dust surface density (note the

fairly low discrepancy between dust masses from physical models, compared to modified blackbody models). The MC11 model requires the highest dust mass and the broken-emissivity model the lowest.

2. We use metallicity and gas measurements to calculate a dust surface density upper limit (assuming all metals in dust) and show that all physical dust models require too much dust over some radial ranges in M101. Only the broken-emissivity modified blackbody model is below the upper limit of $\Sigma_{\mathrm{dust}}^{\max}$ (Figure 12). This finding is dependent on the chosen prescription for the CO-to-H$_2$ conversion factor.

3. To investigate the differences between dust masses and their relationship to the available heavy elements, we renormalized the models via fits to the same SED of the MW diffuse emission, assuming a strict abundance constraint of $M_{\mathrm{dust}}/M_{\mathrm{H}} = 1/150$ (Section 6.2). We derive scaling factors and apply them to the fitted dust surface density, and find renormalized dust mass values lower than $\Sigma_{\mathrm{dust}}^{\max}$ (Figure 12). We find that the choices made to calibrate dust models have a non-negligible impact on the derived dust masses.

To provide the strictest comparison, we do not always use dust models in their fiducial aspect, sometimes assuming a fixed ratio between two dust grain populations. The observational constraints brought by IR emission fitting are used to validate evolution models or derive scaling relations like the dust-to-gas ratio. Our results show that these derived dust properties have systematic uncertainties that should be taken into account. Although there are still systematic uncertainties inherent in the H II region metallicity measurements, resolved metallicity gradients in nearby galaxies can be helpful for testing the opacity calibrations in dust models.

Appendix A
Calibration Details

We present here the details of the calibration methodology used in each physical model and a summary of the calibration constraints in Table A1.

A.1. DL07

DL07 was calibrated using the following constraints. The extinction is described in Weingartner & Draine (2001b) and uses the Fitzpatrick (1999) extinction curves with a normalization of $N_{\mathrm{H}}/E(B - V) = 5.8 \times 10^{21}\,\mathrm{H\,cm}^{-2}$ or $A_V/N_{\mathrm{H}} = 5.3 \times 10^{-22}\,\mathrm{cm}^2$. The high-latitude cirrus emission per H observed by DIRBE (Diffuse Infrared Background Experiment) and FIRAS (Far Infrared Absolute Spectrophotometer; Arendt et al. 1998; Finkbeiner et al. 1999) is used as a reference for the far-IR emission, complemented by mid- and near-IR emission from IRTS (Infrared Telescope in Space; Onaka et al. 1996; Tanaka et al. 1996). Weingartner & Draine (2001b) adopt solar abundances from Grevesse & Sauval (1998), assuming 30% of carbon is in the gas phase. They assume all silicon is depleted and has abundance equal to the solar value. DL07 uses $M_{\mathrm{dust}}/M_{\mathrm{H}} = 1.0 \times 10^{-2}$. The radiation field used in the Draine & Li (2007) model is based on Mathis et al. (1983).

A.2. Compiègne et al. (2011)

MC11 was calibrated using the following constraints. Extinction constraints were taken from Mathis (1990) and Fitzpatrick (1999), including the $R_V = 3.1$ extinction curve in the UV-visible and a normalization of $N_{\mathrm{H}}/E(B - V) = 5.8 \times 10^{21}\,\mathrm{H\,cm}^{-2}$. At $\lambda > 25\,\mu\mathrm{m}$, MC11 use the MW cirrus emission per H observed by COBE-DIRBE and WMAP (integrated in the Herschel and Planck/HFI bands; see MC11). At $\lambda \leqslant 25\,\mu\mathrm{m}$, a compilation of mid-IR observations of high-latitude MW cirrus is used (combining measurements from AROME, DIRBE, and ISOCAM; we refer to reader to the Compiègne et al. paper for details). They scale the emission SED by 0.77 to account for ionized and molecular gas not accounted for in the H column. The allowed dust-phase abundances for C, O, and other dust components come from the difference between solar (or F/G star) abundances and the observed gas-phase abundances. In total, $M_{\mathrm{dust}}/M_{\mathrm{H}} = 1.02 \times 10^{-2}$. MC11 assumes the Mathis et al. (1983, $D_{\mathrm{G}} = 10\,\mathrm{kpc}$) solar neighborhood radiation field to heat the dust grains.

A.3. THEMIS

THEMIS was calibrated using the same constraints as Compiègne et al. (2011) presented in the previous section, with the addition of the far-IR-to-extinction relation $\tau_{250}/E(B - V) = 5.8 \times 10^{-4}$ (Planck Collaboration et al. 2011). In THEMIS, $M_{\mathrm{dust}}/M_{\mathrm{H}} = 7.4 \times 10^{-3}$.

Table A1
Physical Model Calibration Summary

	Draine & Li (2007)	Compiègne et al. (2011)	THEMIS	HD21
Extinction curve	Fitzpatrick (1999)	Mathis (1990)	Mathis (1990)	Fitzpatrick et al. (2019)
				Schlafly et al. (2016)
				Hensley & Draine (2020)
$N_{\rm H}/E(B-V)$	5.8×10^{21} H cm^{-2}	5.8×10^{21} H cm^{-2}	5.8×10^{21} H cm^{-2}[a]	8.8×10^{21} cm^{-2} mag^{-1}
Emission spectrum	Onaka et al. (1996)	compiled in Compiègne et al. (2011)	compiled in Compiègne et al. (2011)	Planck Collaboration Int. XVII (2014)
	Tanaka et al. (1996)			Planck Collaboration Int. XVII (2015)
	Arendt et al. (1998)			Planck Collaboration XI (2020)
	Finkbeiner et al. (1999)			
$M_{\rm d}/M_{\rm H}$	1.0×10^{-2}	1.02×10^{-2}	7.4×10^{-3}	1.0×10^{-2}
Radiation Field	Mathis et al. (1983)	Mathis et al. (1983)	Mathis et al. (1983)	Draine (2011)
Renormalization: emission constraint only from Compiègne et al. (2011)[b] and forcing $M_{\rm d}/M_{\rm H} = 6.6 \times 10^{-3}$				
$U_{\rm min}^{\rm MW}$	0.6	1.0	1.0	1.6
Normalization factor	3.1	2.1	1.5	2.5

Notes. All models share $R_V = 3.1$.
[a] Additional constraint: $\tau_{250}/E(B-V) = 5.8 \times 10^{-4}$ (Planck Collaboration et al. 2011).
[b] Corrected for molecular gas only, not ionized gas.

A.4. B. S. Hensley & B. T. Draine (2021, in preparation)

The full set of observational constraints used to develop the model is described in Hensley & Draine (2021). In brief, the extinction curve is primarily a synthesis of those of Fitzpatrick et al. (2019) in the UV and optical, Schlafly et al. (2016) in the optical and near-infrared, and Hensley & Draine (2020) in the mid-infrared. The normalization $N_{\rm H}/E(B-V) = 8.8 \times 10^{21}$ cm^{-2} mag^{-1} is used to normalize extinction to the hydrogen column (Lenz et al. 2017). The infrared emission in both total intensity and polarization are based on the analyses presented in Planck Collaboration Int. XVII (2014, 2015), and Planck Collaboration XI (2020), including the normalization to $N_{\rm H}$. The solid phase interstellar abundances are re-determined in Hensley & Draine (2021)

using a set of solar abundances (Asplund et al. 2009; Scott et al. 2015a, 2015b), a measurement of Galactic chemical enrichment from solar twin studies (Bedell et al. 2018), and determination of the gas-phase abundances from absorption spectroscopy (Jenkins 2009). $M_{\rm dust}/M_{\rm H} = 1.0 \times 10^{-2}$ in this model. HD21 assumes the same radiation field as the DL07 model to heat the dust grains, with updates from Draine (2011).
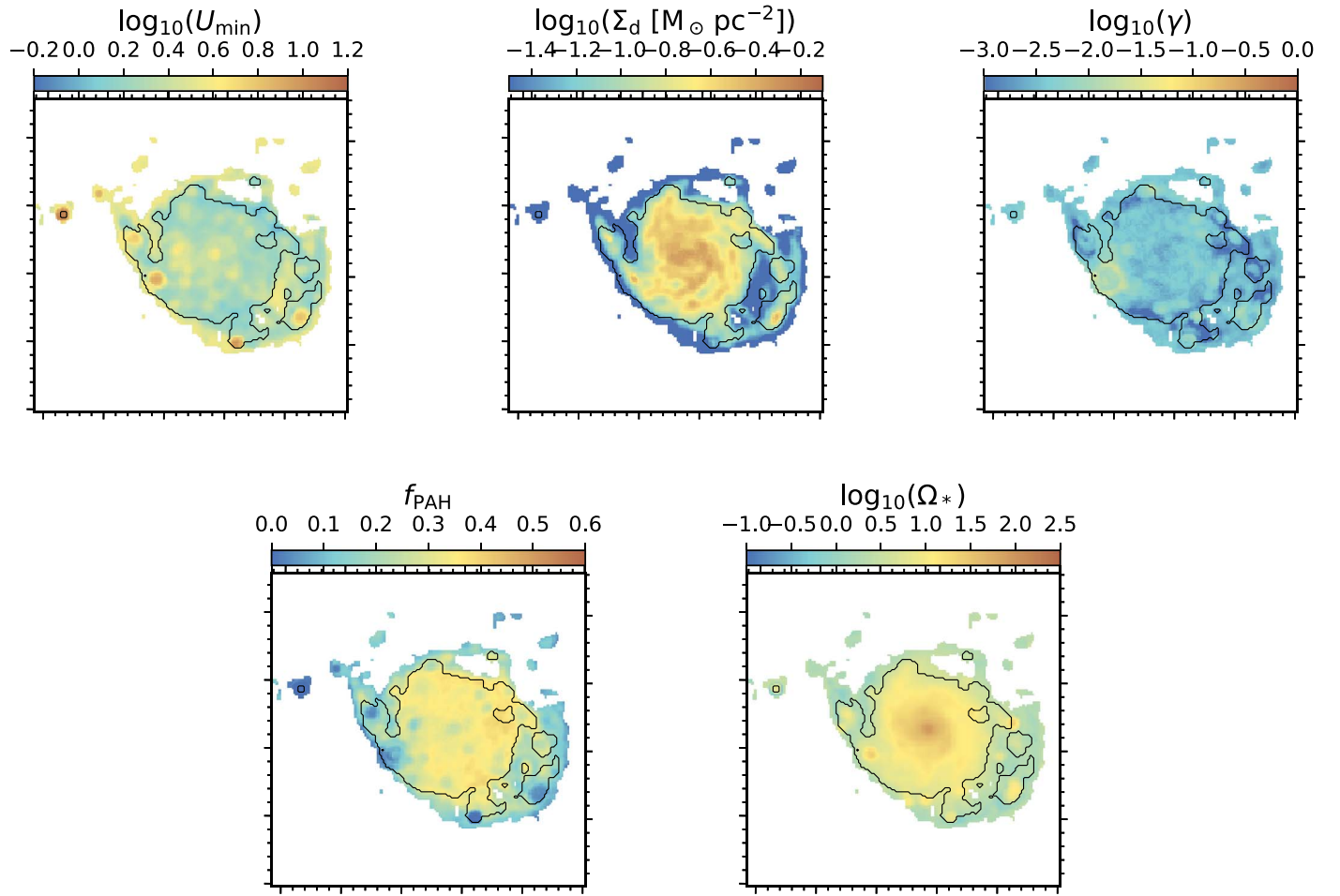
Appendix B
Fitted Parameter Maps

We present the spatial variations of the fitted parameters for all six models, in Figures B1–B5. The contours mark the 3σ detection threshold. We use the same scale for identical parameters, when possible.
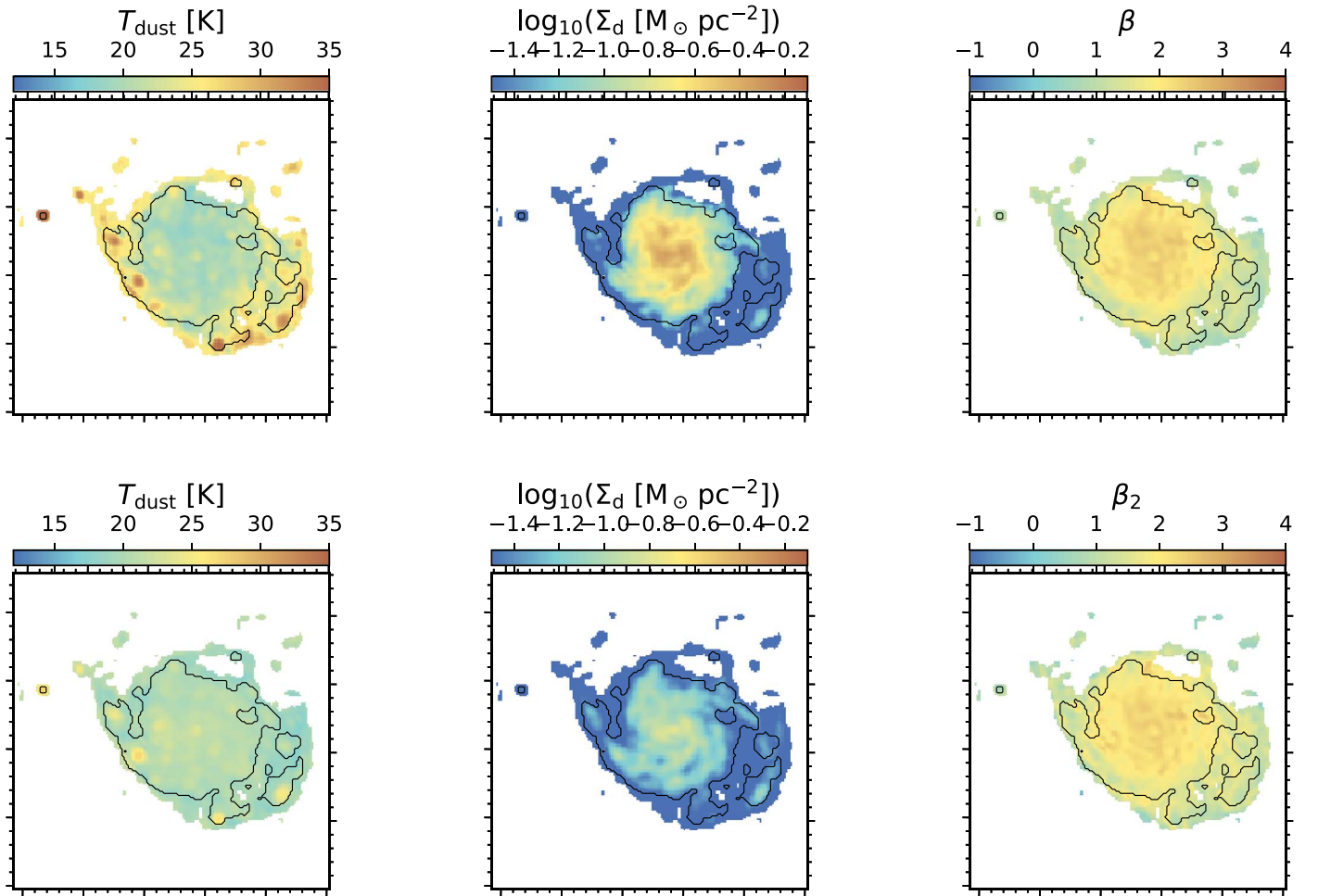
Figure B1. Maps of fitted parameters. Top: simple-emissivity model, dust temperature ($T_{\rm dust}$), total dust surface density ($\Sigma_{\rm dust}$) and spectral index (β). Bottom: broken-emissivity model, dust temperature ($T_{\rm dust}$), total dust surface density ($\Sigma_{\rm dust}$) and second spectral index (β_2); the breaking wavelength is fixed ($\lambda_{\rm c} = 300~\mu$m) as well as the first spectral index ($\beta = 2$).
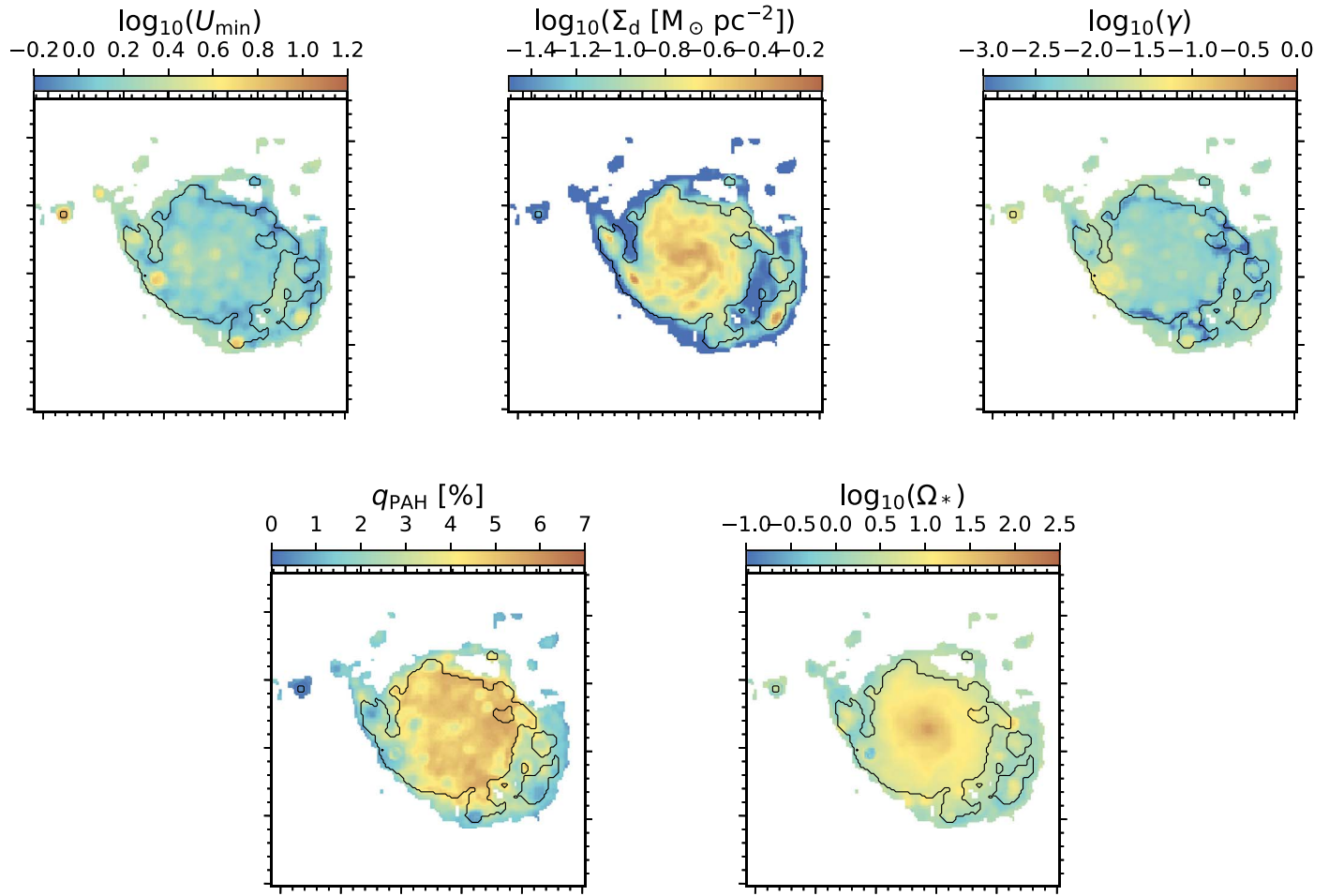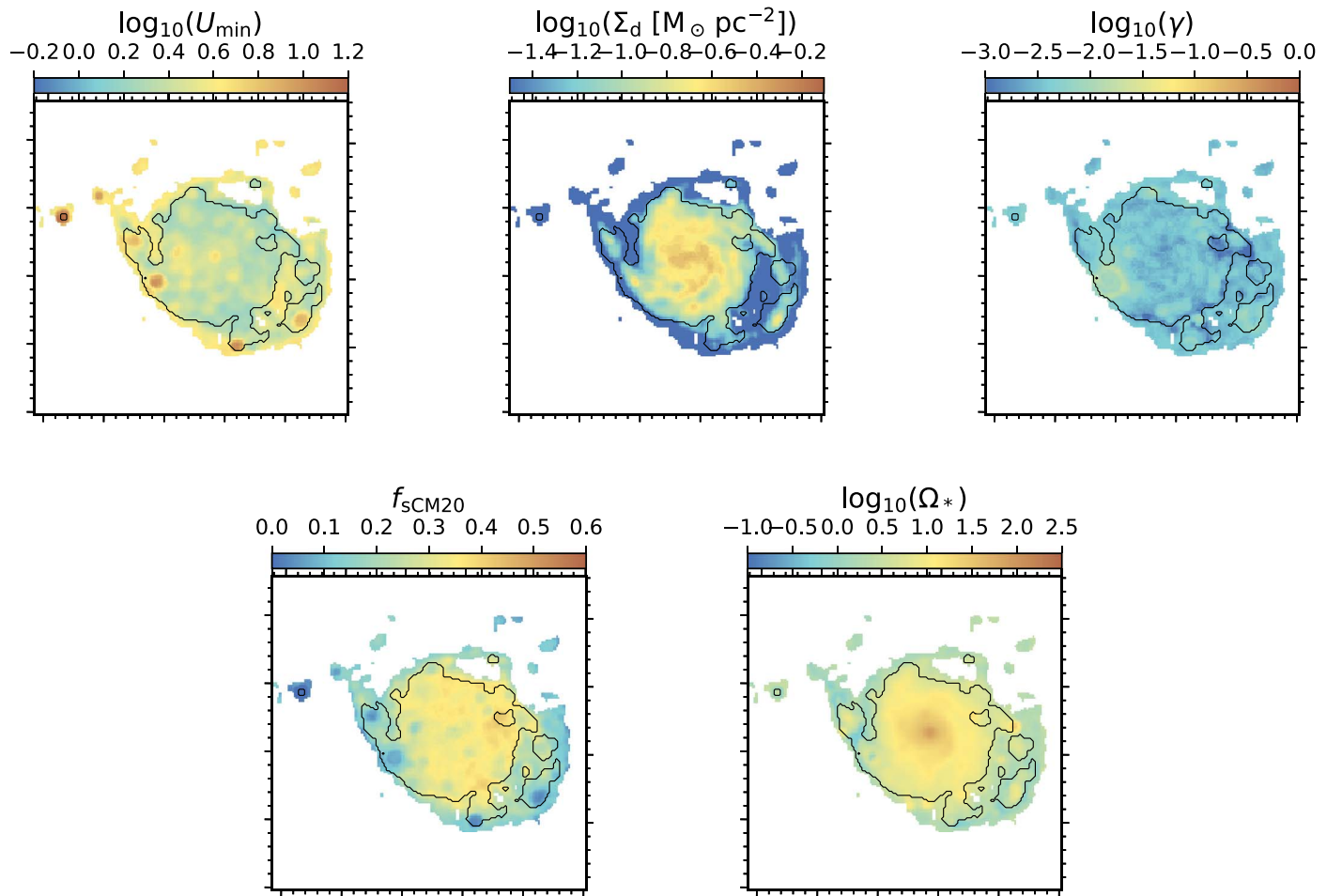
Figure B2. Maps of the fitted parameters for the Draine & Li (2007) model: minimum radiation field (U_{min}), total dust surface density (Σ_{dust}), fraction of dust mass heated by a power-law distribution of the radiation field (γ), PAH fraction (mass in grains with less than 10^3 C atoms, q_{PAH}), and scaling parameter of surface brightness (5000 K blackbody, Ω_*).

Figure B3. Maps of the fitted parameters for the Compiègne et al. (2011) model: minimum radiation field (U_{min}), total dust surface density (Σ_{dust}), fraction of dust mass heated by a power-law distribution of the radiation field (γ), PAH fraction (with respect to total dust mass, f_{PAH}), and scaling parameter of surface brightness (5000 K blackbody, Ω_*).

Figure B4. Maps of the fitted parameters for the Jones et al. (2013) model: minimum radiation field (U_{min}), total dust surface density (Σ_{dust}), fraction of dust mass heated by a power-law distribution of the radiation field (γ), sCM20 fraction (small carbon grains, f_{sCM20}), and scaling parameter of surface brightness (5000 K blackbody, Ω_*).
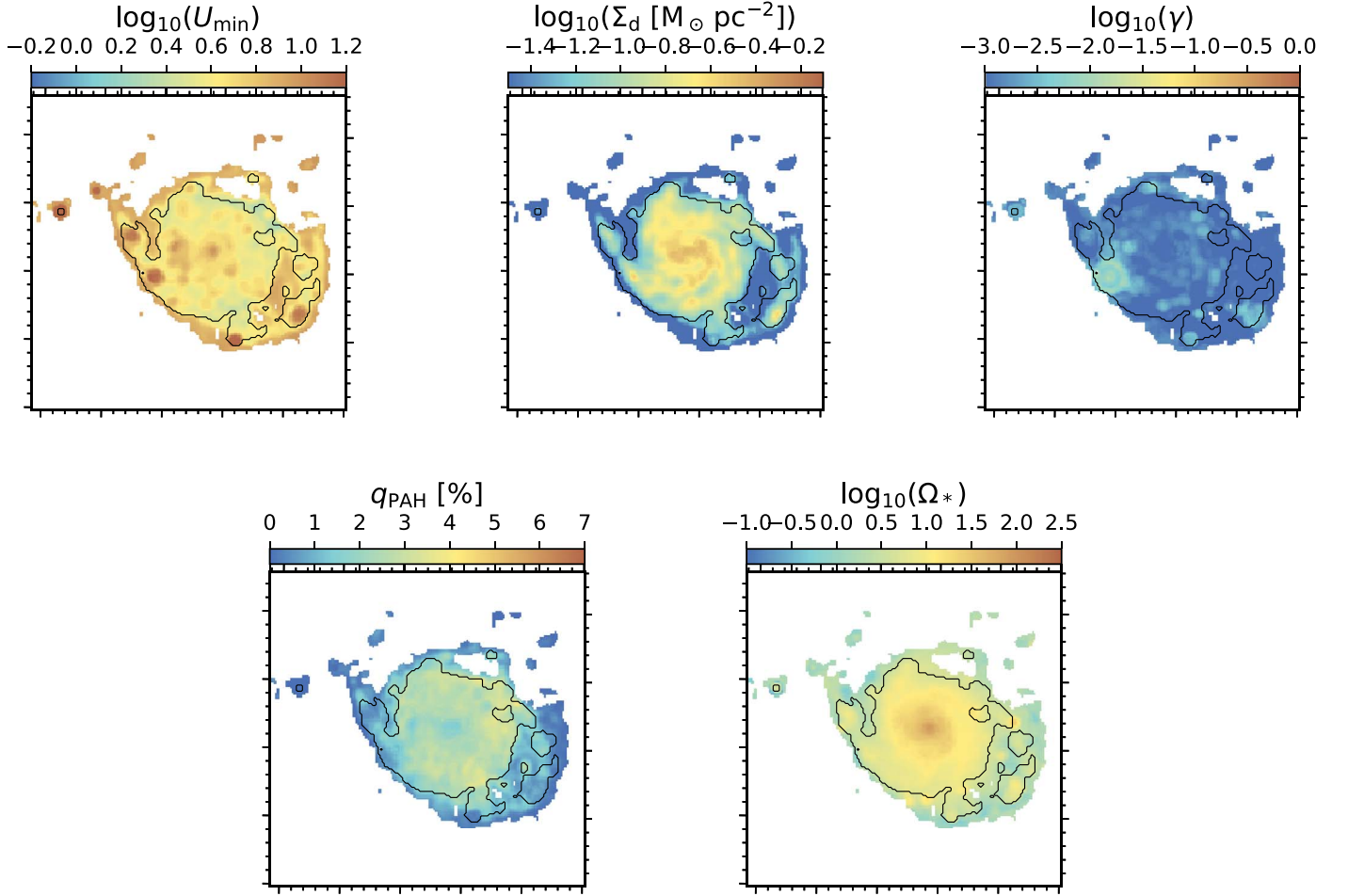
Figure B5. Maps of the fitted parameters for the HD21 model: minimum radiation field ($U_{\min}$), total dust surface density (Σ_{dust}), fraction of dust mass heated by a power-law distribution of the radiation field (γ), PAH fraction (mass in grains with less than 10^3 C atoms, q_{PAH}), and scaling parameter of surface brightness (5000 K blackbody, Ω_*).

Appendix C
Residual Maps

We present the spatial variations of the fractional residuals (Data–Model)/Model for all six models, in Figures C1–C5. The contours mark the 3σ detection threshold. The so-called "submillimeter" excess is visible in most maps at SPIRE 500 (blue shade).
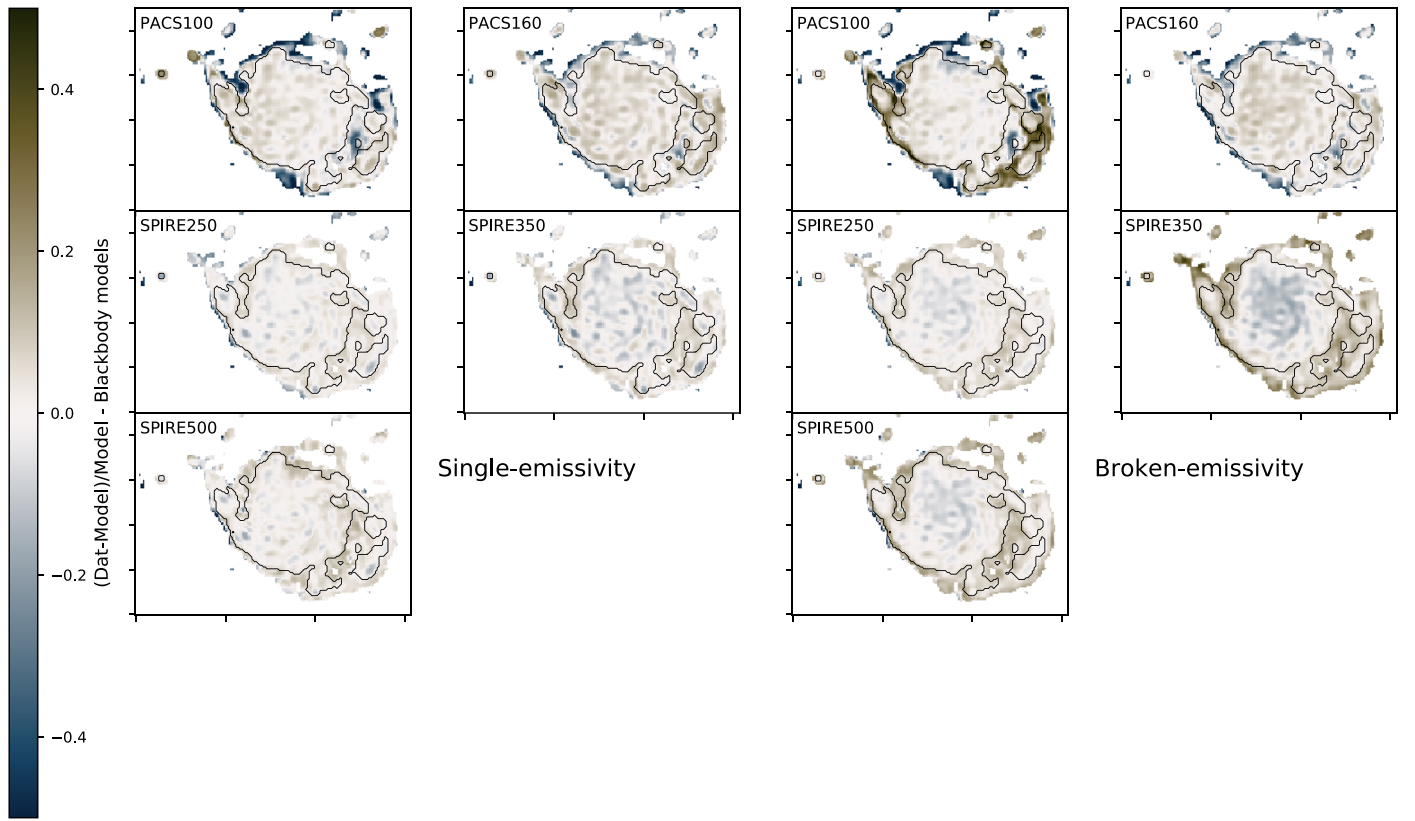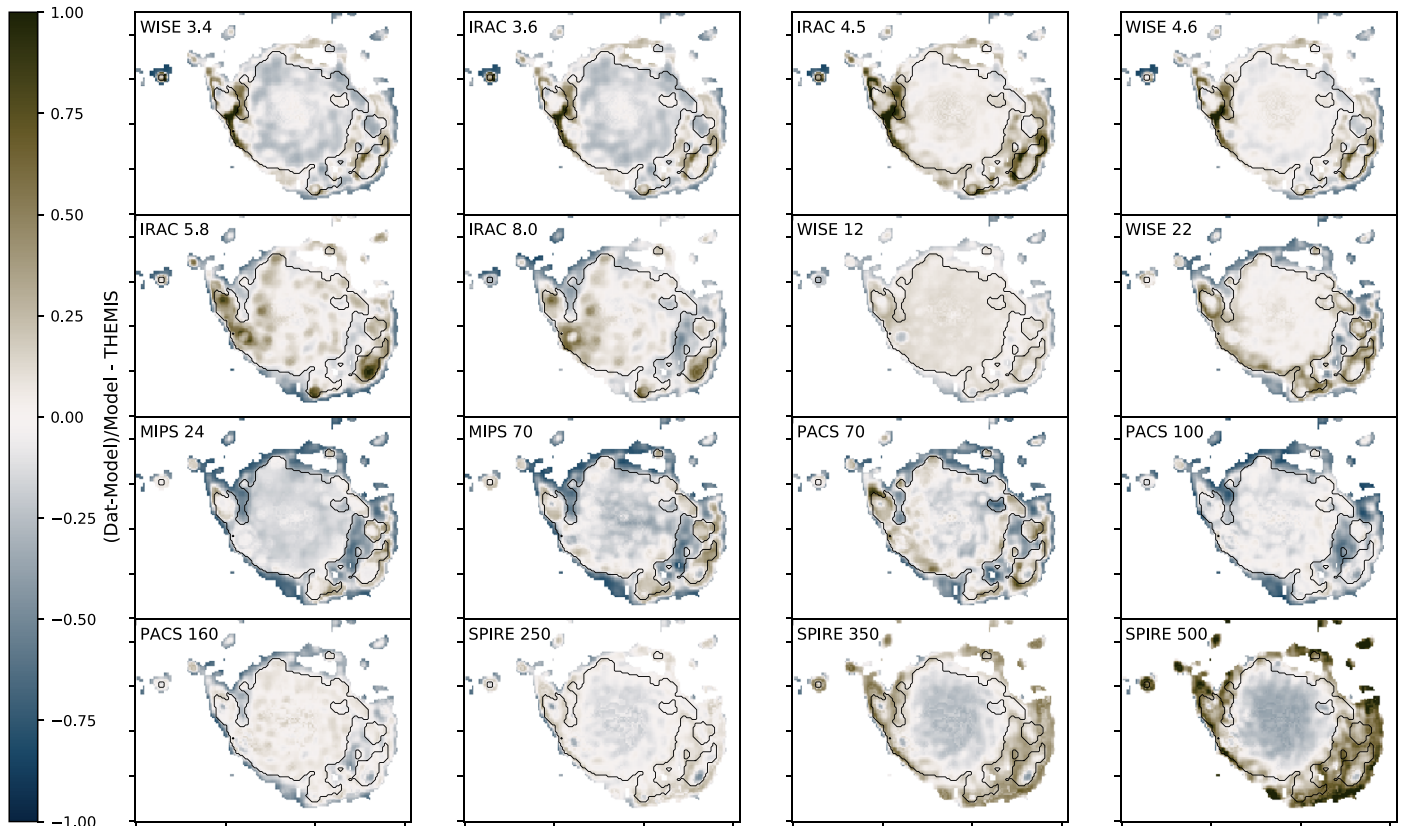
Figure C1. Maps of the fractional residuals for the simple-emissivity and broken-emissivity models.
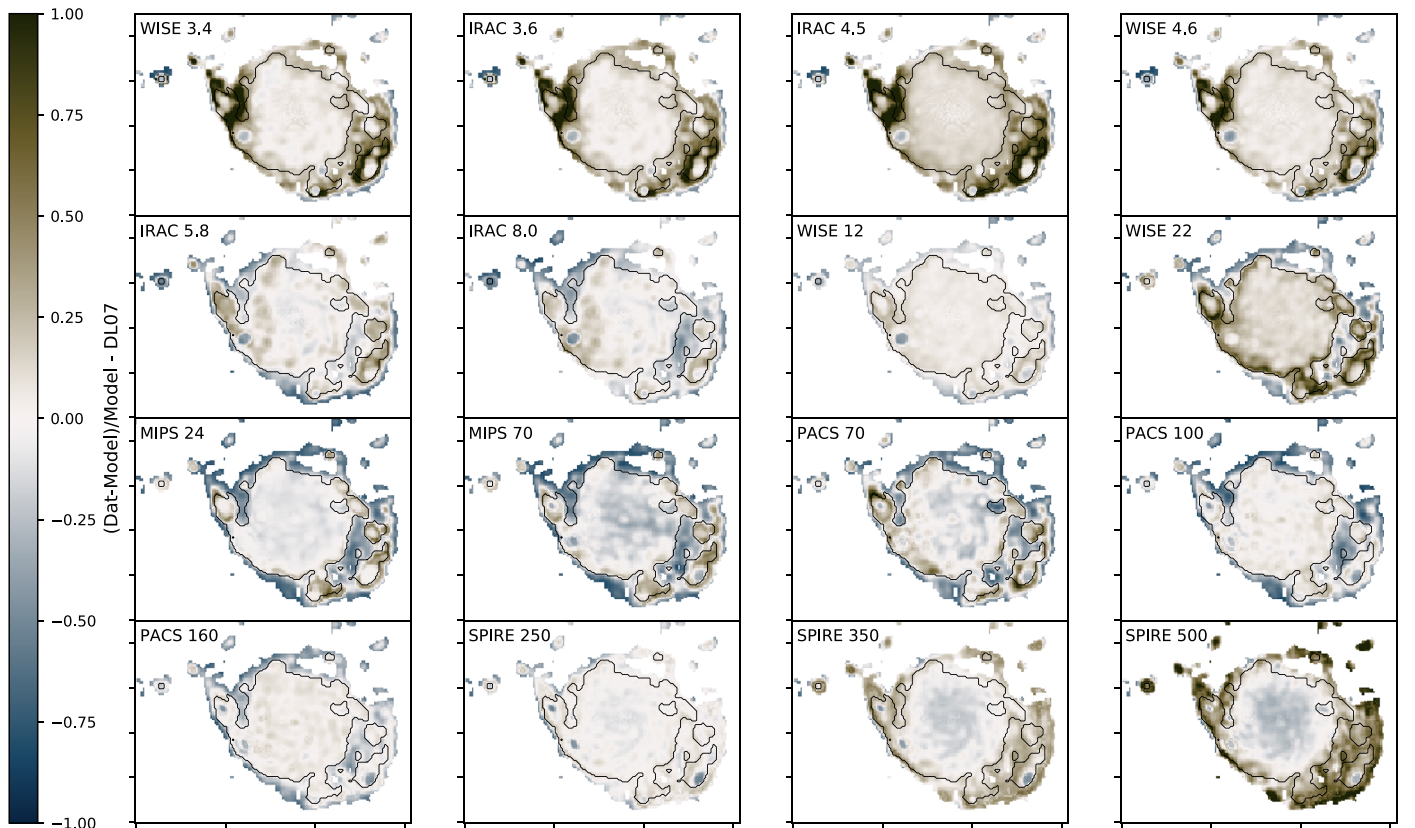
Figure C2. Maps of the fractional residuals for the Draine & Li (2007) model.
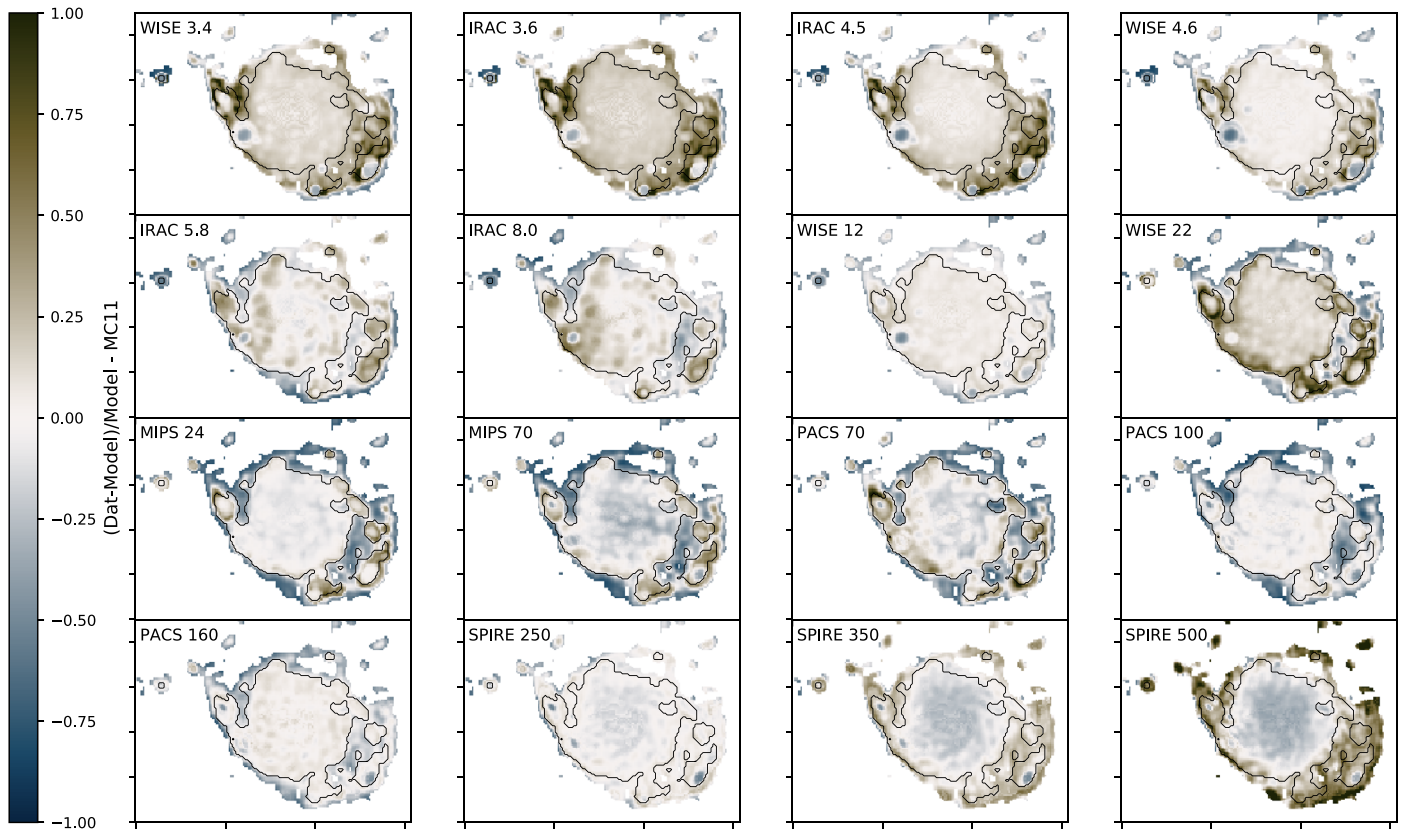
Figure C3. Maps of the fractional residuals for the Compiègne et al. (2011) model.

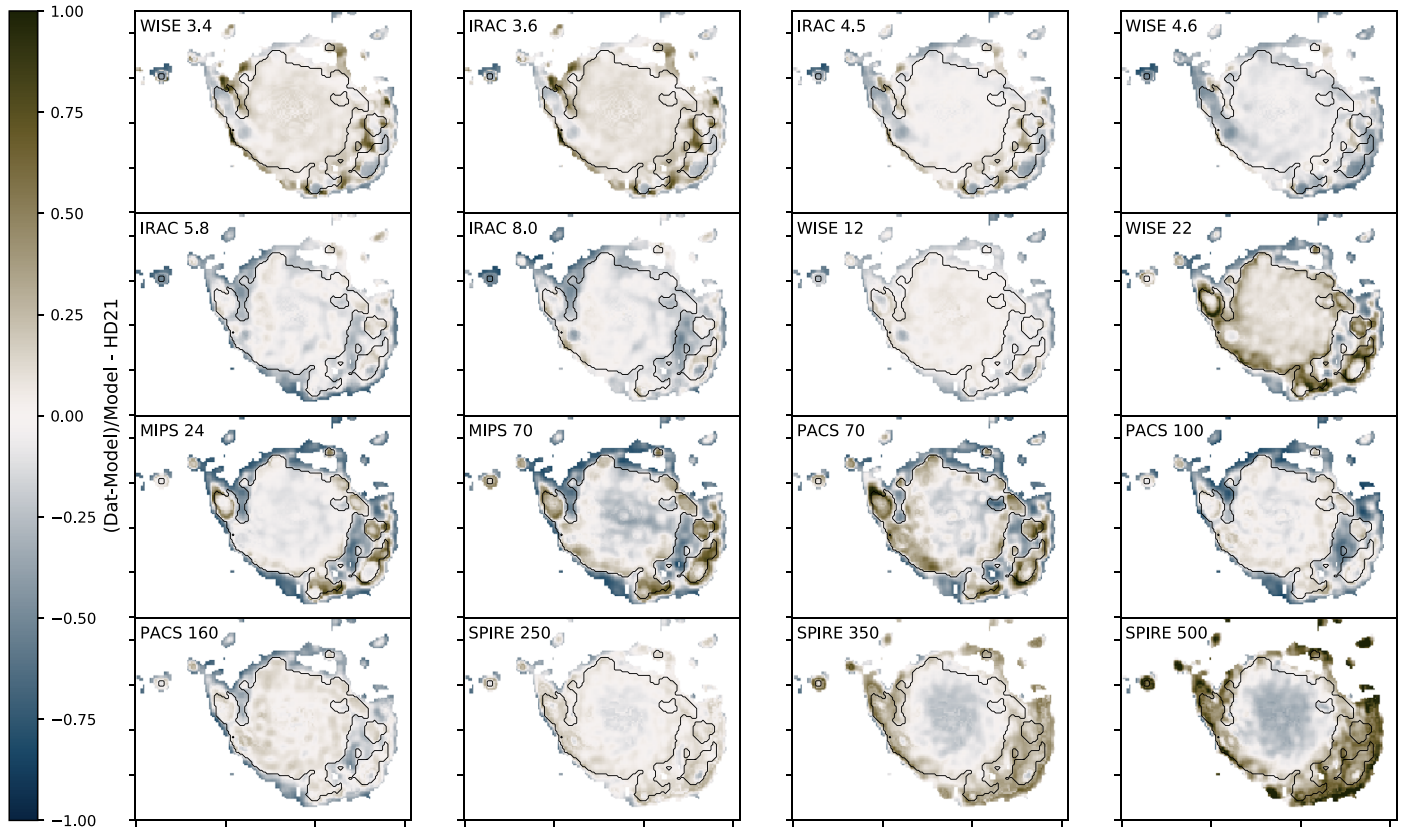**Figure C4.** Maps of the fractional residuals for the Jones et al. (2013) model.

Figure C5. Maps of the fractional residuals for the HD21 model.

Appendix D
Fits Quality

In Figure D1, we show the relative quality of the fits between each model. The value displayed in the maximum likelihood, in arbitrary units. The simple-emissivity and broken-emissivity models show the least dynamic range but never reach the highest values of the physical models. For the physical models, we can clearly see the H II regions showing fits with low confidence, likely related to the issues mentioned in Section 5.7.
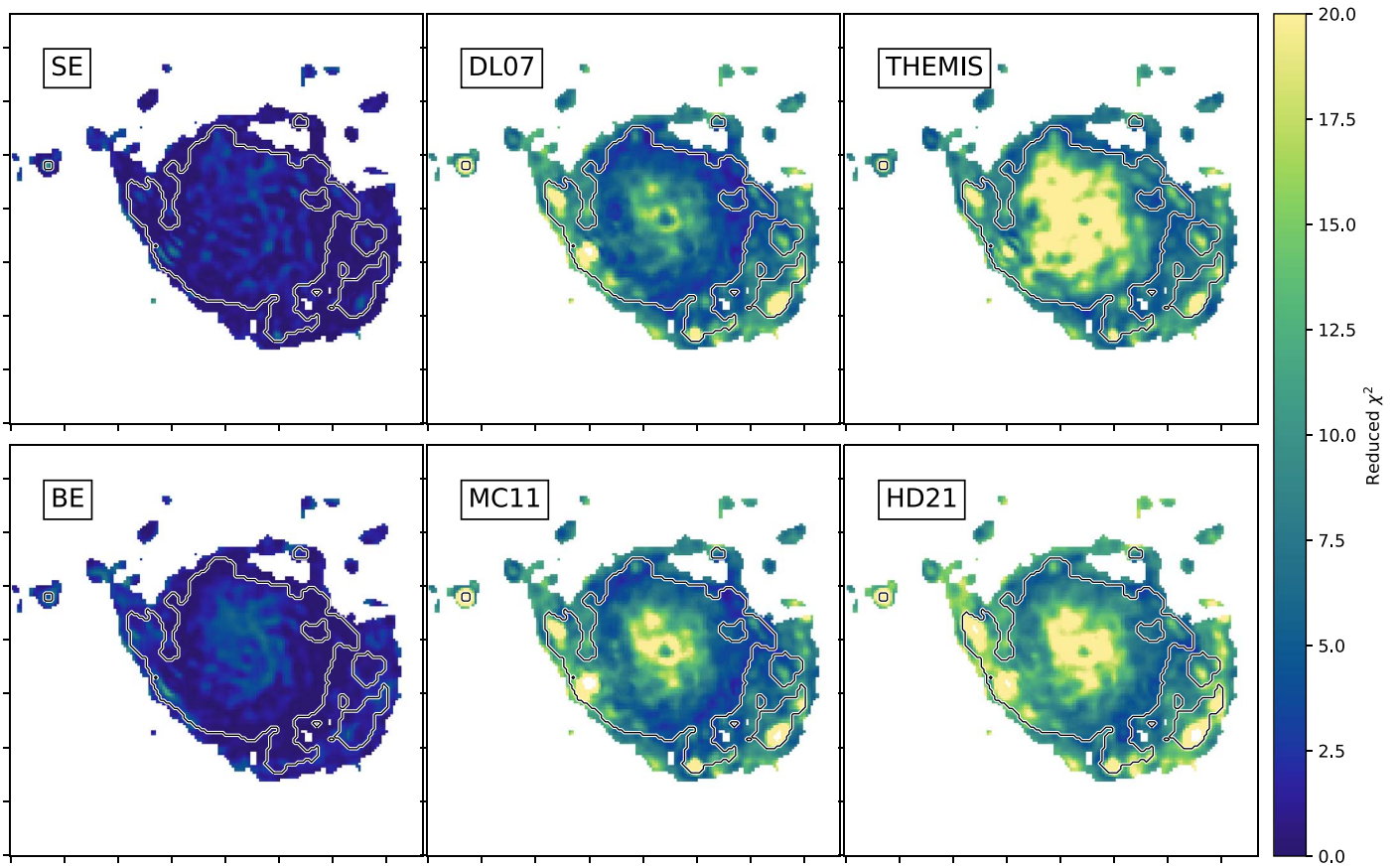
Figure D1. Maps of the reduced χ^2 in each pixel. The H II regions show the lowest confidence for the physical models, while the modified blackbodies show good fits on the entire disk. The contour marks the 3σ detection threshold.

ORCID iDs

Jérémy Chastenet ⓘ https://orcid.org/0000-0002-5235-5589
Karin Sandstrom ⓘ https://orcid.org/0000-0002-4378-8534
I-Da Chiang (江宜達) ⓘ https://orcid.org/0000-0003-2551-7148
Brandon S. Hensley ⓘ https://orcid.org/0000-0001-7449-4638
Bruce T. Draine ⓘ https://orcid.org/0000-0002-0846-936X
Karl D. Gordon ⓘ https://orcid.org/0000-0001-5340-6774
Eric W. Koch ⓘ https://orcid.org/0000-0001-9605-780X
Adam K. Leroy ⓘ https://orcid.org/0000-0002-2545-1700
Dyas Utomo ⓘ https://orcid.org/0000-0003-4161-2639
Thomas G. Williams ⓘ https://orcid.org/0000-0002-0012-2142

References

Adami, O.-A., Rodriguez, L., Poglitsch, A., et al. 2019, ApOpt, 58, 398
Allamandola, L. J., Tielens, A. G. G. M., & Barker, J. R. 1985, ApJL, 290, L25
Aniano, G., Draine, B. T., Calzetti, D., et al. 2012, ApJ, 756, 138
Aniano, G., Draine, B. T., Gordon, K. D., & Sandstrom, K. 2011, PASP, 123, 1218
Aniano, G., Draine, B. T., Hunt, L. K., et al. 2020, ApJ, 889, 150
Arendt, R. G., Odegard, N., Weiland, J. L., et al. 1998, ApJ, 508, 74
Asplund, M., Grevesse, N., Sauval, A. J., & Scott, P. 2009, ARA&A, 47, 481
Astropy Collaboration, Price-Whelan, A. M., Sipőcz, B. M., et al. 2018, AJ, 156, 123
Astropy Collaboration, Robitaille, T. P., Tollerud, E. J., et al. 2013, A&A, 558, A33
Baes, M., Trčka, A., & Camps, P. 2020, MNRAS, 494, 2912
Balog, Z., Müller, T., Nielbock, M., et al. 2013, ExA, 37, 129
Bedell, M., Bean, J. L., Meléndez, J., et al. 2018, ApJ, 865, 68
Bendo, G. J., Griffin, M. J., Bock, J. J., et al. 2013, MNRAS, 433, 3062
Berg, D. A., Pogge, R. W., Skillman, E. D., et al. 2020, ApJ, 893, 96
Berta, S., Lutz, D., Genzel, R., Förster-Schreiber, N. M., & Tacconi, L. J. 2016, A&A, 587, A73
Bianchi, S. 2013, A&A, 552, A89
Bolatto, A. D., Wolfire, M., & Leroy, A. K. 2013, ARA&A, 51, 207
Boquien, M., Burgarella, D., Roehlly, Y., et al. 2019, A&A, 622, A103
Boulanger, F., Abergel, A., Bernard, J. P., et al. 1996, A&A, 312, 256
Bron, E., Le Bourlot, J., & Le Petit, F. 2014, A&A, 569, A100
Byrne, L., Christensen, C., Tsekitsidis, M., Brooks, A., & Quinn, T. 2019, ApJ, 871, 213
Castellanos, P., Candian, A., Andrews, H., & Tielens, A. G. G. M. 2018, A&A, 616, A167
Chastenet, J., Bot, C., Gordon, K. D., et al. 2017, A&A, 601, A55
Chastenet, J., Sandstrom, K., Chiang, I. D., et al. 2019, ApJ, 876, 62
Chiang, I. D., Sandstrom, K. M., Chastenet, J., et al. 2018, ApJ, 865, 117
Chiang, I.-D., Sandstrom, K. M., Chastenet, J., et al. 2021, ApJ, 907, 29
Compiègne, M., Verstraete, L., Jones, A., et al. 2011, A&A, 525, A103
Croxall, K. V., Pogge, R. W., Berg, D. A., Skillman, E. D., & Moustakas, J. 2016, ApJ, 830, 4
Croxall, K. V., Smith, J. D., Wolfire, M. G., et al. 2012, ApJ, 747, 81
Dale, D. A., Cohen, S. A., Johnson, L. C., et al. 2009, ApJ, 703, 517
Dale, D. A., Helou, G., Contursi, A., Silbermann, N. A., & Kolhatkar, S. 2001, ApJ, 549, 215
Davies, J. I., Baes, M., Bianchi, S., et al. 2017, PASP, 129, 044102
de Blok, W. J. G., Walter, F., Brinks, E., et al. 2008, AJ, 136, 2648
De Looze, I., Lamperti, I., Saintonge, A., et al. 2020, MNRAS, 496, 3668
De Vis, P., Jones, A., Viaene, S., et al. 2019, A&A, 623, A5
Demyk, K., Meny, C., Lu, X. H., et al. 2017, A&A, 600, A123
Desert, F. X., Boulanger, F., & Puget, J. L. 1990, A&A, 500, 313
Desert, F. X., Boulanger, F., & Shore, S. N. 1986, A&A, 160, 295
Draine, B. T. 2003, ApJ, 598, 1026
Draine, B. T. 2011, Physics of the Interstellar and Intergalactic Medium (Princeton, NJ: Princeton Univ. Press)
Draine, B. T. 2016, ApJ, 831, 109
Draine, B. T., Aniano, G., Krause, O., et al. 2014, ApJ, 780, 172
Draine, B. T., & Hensley, B. S. 2021, ApJ, 909, 94

Draine, B. T., & Lee, H. M. 1984, ApJ, 285, 89
Draine, B. T., & Li, A. 2001, ApJ, 551, 807
Draine, B. T., & Li, A. 2007, ApJ, 657, 810
Eales, S., Smith, M. W. L., Auld, R., et al. 2012, ApJ, 761, 168
Engelbracht, C. W., Blaylock, M., Su, K. Y. L., et al. 2007, PASP, 119, 994
Fanciullo, L., Kemper, F., Scicluna, P., Dharmawardena, T. E., & Srinivasan, S. 2020, MNRAS, 499, 4666
Fazio, G. G., Hora, J. L., Allen, L. E., et al. 2004, ApJS, 154, 10
Finkbeiner, D. P., Davis, M., & Schlegel, D. J. 1999, ApJ, 524, 867
Fitzpatrick, E. L. 1999, PASP, 111, 63
Fitzpatrick, E. L., Massa, D., Gordon, K. D., Bohlin, R., & Clayton, G. C. 2019, ApJ, 886, 108
Fumagalli, M., Krumholz, M. R., & Hunt, L. K. 2010, ApJ, 722, 919
Galametz, M., Albrecht, M., Kennicutt, R., et al. 2014, MNRAS, 439, 2542
Galliano, F., Galametz, M., & Jones, A. P. 2018, ARA&A, 56, 673
Galliano, F., Hony, S., Bernard, J. P., et al. 2011, A&A, 536, A88
Gordon, K. D., Engelbracht, C. W., Fadda, D., et al. 2007, PASP, 119, 1019
Gordon, K. D., Roman-Duval, J., Bot, C., et al. 2014, ApJ, 797, 85
Grevesse, N., & Sauval, A. J. 1998, SSRv, 85, 161
Griffin, M. J., Abergel, A., Abreu, A., et al. 2010, A&A, 518, L3
Groves, B. A., Schinnerer, E., Leroy, A., et al. 2015, ApJ, 799, 96
Guillet, V., Fanciullo, L., Verstraete, L., et al. 2018, A&A, 610, A16
Harper, D. A., Runyan, M. C., Dowell, C. D., et al. 2018, JAI, 7, 1840008
Hensley, B. S., & Draine, B. T. 2017, ApJ, 836, 179
Hensley, B. S., & Draine, B. T. 2020, ApJ, 895, 38
Hensley, B. S., & Draine, B. T. 2021, ApJ, 906, 73
Hunter, J. D. 2007, CSE, 9, 90
Jenkins, E. B. 2009, ApJ, 700, 1299
Jones, A. P., Fanciullo, L., Köhler, M., et al. 2013, A&A, 558, A62
Jones, A. P., Köhler, M., Ysard, N., Bocchio, M., & Verstraete, L. 2017, A&A, 602, A46
Kemper, F., Vriend, W. J., & Tielens, A. G. G. M. 2004, ApJ, 609, 826
Kennicutt, R. C., Calzetti, D., Aniano, G., et al. 2011, PASP, 123, 1347
Köhler, M., Jones, A., & Ysard, N. 2014, A&A, 565, L9
Kreckel, K., Ho, I. T., Blanc, G. A., et al. 2019, ApJ, 887, 80
Leger, A., & Puget, J. L. 1984, A&A, 500, 279
Lenz, D., Hensley, B. S., & Doré, O. 2017, ApJ, 846, 38
Leroy, A. K., Sandstrom, K. M., Lang, D., et al. 2019, ApJS, 244, 24
Leroy, A. K., Walter, F., Bigiel, F., et al. 2009, AJ, 137, 4670
Leroy, A. K., Walter, F., Brinks, E., et al. 2008, AJ, 136, 2782
Li, A., & Draine, B. T. 2001, ApJ, 554, 778
Lianou, S., Barmby, P., Mosenkov, A. A., Lehnert, M., & Karczewski, O. 2019, A&A, 631, A38
Makarov, D., Prugniel, P., Terekhova, N., Courtois, H., & Vauglin, I. 2014, A&A, 570, A13
Mathis, J. S. 1990, ARA&A, 28, 37
Mathis, J. S., Mezger, P. G., & Panagia, N. 1983, A&A, 500, 259
Mathis, J. S., Rumpl, W., & Nordsieck, K. H. 1977, ApJ, 217, 425
Moustakas, J., Kennicutt, R. C. J., Tremonti, C. A., et al. 2010, ApJS, 190, 233
Müller, T., Nielbock, M., Balog, Z., Klaas, U., & Vilenius, E. 2011, PACS Photometer—Point-Source Flux Calibration, Technical Report, PICC-ME-TN-037, Herschel
Mutschke, H., & Mohr, P. 2019, A&A, 625, A61
Nanni, A., Burgarella, D., Theulé, P., Côté, B., & Hirashita, H. 2020, A&A, 641, A168
Nersesian, A., Xilouris, E. M., Bianchi, S., et al. 2019, A&A, 624, A80

Onaka, T., Yamamura, I., Tanabe, T., Roellig, T. L., & Yuen, L. 1996, PASJ, 48, L59
Ott, S. 2010, in ASP Conf. Ser. 434, Astronomical Data Analysis Software and Systems XIX, ed. Y. Mizumoto, K.-I. Morita, & M. Ohishi (San Francisco, CA: ASP), 139
Paradis, D., Mény, C., Juvela, M., Noriega-Crespo, A., & Ristorcelli, I. 2019, A&A, 627, A15
Peimbert, A., & Peimbert, M. 2010, ApJ, 724, 791
Pilbratt, G. L., Riedinger, J. R., Passvogel, T., et al. 2010, A&A, 518, L1
Planck Collaboration, Abergel, A., & Ade, P. A. R. 2011, A&A, 536, A24
Planck Collaboration Int. XVII 2014, A&A, 566, A55
Planck Collaboration Int. XVII 2015, A&A, 576, A107
Planck Collaboration XI 2020, A&A, 641, A11
Poglitsch, A., Waelkens, C., Geis, N., et al. 2010, A&A, 518, L2
Reach, W. T., Megeath, S. T., Cohen, M., et al. 2005, PASP, 117, 978
Relaño, M., Lisenfeld, U., Hou, K. C., et al. 2020, A&A, 636, A18
Rémy-Ruyer, A., Madden, S. C., Galliano, F., et al. 2014, A&A, 563, A31
Richey, C. R., Kinzer, R. E., Cataldo, G., et al. 2013, ApJ, 770, 46
Rieke, G. H., Young, E. T., Engelbracht, C. W., et al. 2004, ApJS, 154, 25
Robitaille, T. 2019, APLpy v2.0: The Astronomical Plotting Library in Python, Zenodo, doi:10.5281/zenodo.2567476
Robitaille, T., & Bressert, E. 2012, APLpy: Astronomical Plotting Library in Python, Astrophysics Source Code Library, ascl:1208.017
Roussel, H. 2013, PASP, 125, 1126
Sandstrom, K. M., Bolatto, A. D., Draine, B. T., Bot, C., & Stanimirović, S. 2010, ApJ, 715, 701
Sandstrom, K. M., Leroy, A. K., Walter, F., et al. 2013, ApJ, 777, 5
Schlafly, E. F., Meisner, A. M., Stutz, A. M., et al. 2016, ApJ, 821, 78
Schruba, A., Leroy, A. K., Walter, F., et al. 2011, AJ, 142, 37
Scott, P., Asplund, M., Grevesse, N., Bergemann, M., & Sauval, A. J. 2015a, A&A, 573, A26
Scott, P., Grevesse, N., Asplund, M., et al. 2015b, A&A, 573, A25
Scoville, N., Lee, N., Vanden Bout, P., et al. 2017, ApJ, 837, 150
Skillman, E. D., Berg, D. A., Pogge, R. W., et al. 2020, ApJ, 894, 138
Sofue, Y., Tutui, Y., Honma, M., et al. 1999, ApJ, 523, 136
Tanaka, M., Matsumoto, T., Murakami, H., et al. 1996, PASJ, 48, L53
Tchernyshyov, K., Meixner, M., Seale, J., et al. 2015, ApJ, 811, 78
Thi, W. F., Hocuk, S., Kamp, I., et al. 2020, A&A, 634, A42
Tully, R. B., Rizzi, L., Shaya, E. J., et al. 2009, AJ, 138, 323
Utomo, D., Chiang, I. D., Leroy, A. K., Sandstrom, K. M., & Chastenet, J. 2019, ApJ, 874, 141
Van Der Walt, S., Colbert, S. C., & Varoquaux, G. 2011, CSE, 13, 22
Vílchez, J. M., Relaño, M., Kennicutt, R., et al. 2019, MNRAS, 483, 4968
Virtanen, P., Gommers, R., Oliphant, T. E., et al. 2020, NatMe, 17, 261
Wakelam, V., Bron, E., Cazaux, S., et al. 2017, MolAs, 9, 1
Walter, F., Brinks, E., de Blok, W. J. G., et al. 2008, AJ, 136, 2563
Weingartner, J. C., & Draine, B. T. 2001a, ApJS, 134, 263
Weingartner, J. C., & Draine, B. T. 2001b, ApJ, 548, 296
Werner, M. W., Roellig, T. L., Low, F. J., et al. 2004, ApJS, 154, 1
Wolfire, M. G., Hollenbach, D., McKee, C. F., Tielens, A. G. G. M., & Bakes, E. L. O. 1995, ApJ, 443, 152
Wright, E. L., Eisenhardt, P. R. M., Mainzer, A. K., et al. 2010, AJ, 140, 1868
Ysard, N., Köhler, M., Jones, A., et al. 2015, A&A, 577, A110
Zaritsky, D., Kennicutt, Robert, C., & Huchra, J. P, J. 1994, ApJ, 420, 87
Zeegers, S. T., Costantini, E., Rogantini, D., et al. 2019, A&A, 627, A16
Zubko, V., Dwek, E., & Arendt, R. G. 2004, ApJS, 152, 211